Available online at www.sciencedirect.com
ScienceDirect
Trans. Nonferrous Met. Soc. China 32(2022) 2451−2479
Transactions of Nonferrous Metals Society of China
www.tnmsc.cn

Recent progress on apparatus development and in situ observation of metal solidification processes via synchrotron radiation X-ray imaging: A review

Wen-quan LU*, Nai-fang ZHANG*, Zong-ye DING, Qiao-dan HU, Jian-guo LI

School of Materials Science and Engineering, Shanghai Jiao Tong University, Shanghai 200240, China

Received 30 August 2021; accepted 28 April 2022

Abstract: The solidification process of metals plays a critical role in their final microstructure and, correspondingly, in their performance. It is therefore important to probe the solidification behavior of metals using advanced in situ techniques. Synchrotron radiation X-ray imaging is one of the most powerful techniques to observe the solidification process of metals directly. Here, we review the development of the solidification apparatus, including the directional solidification device, resistance furnace, multi-field coupling device, semisolid forming device, aerodynamic levitation apparatus, and laser additive manufacturing apparatus. We highlight the recent research progress on the use of synchrotron radiation X-ray imaging to reveal the solidification behavior of metals in the above circumstances. The future perspectives of synchrotron radiation X-ray imaging in metal research are discussed. Further development of this technique will contribute to improve the understanding of the solidification process of metals and other types of materials at different scales.

Key words: synchrotron radiation imaging; in situ observation; solidification behavior; solidification apparatus; metal

1 Introduction

Metals are the muscles and bones of modern industry. They are widely used in machinery, automotive industry, electronics, vessels, aerospace industry, architecture, and energy, almost in every aspect of human life [1,2]. Metals always undergo melting and solidification during various forming processes, such as additive manufacturing, welding, and casting [3,4]. Their final microstructure, and consequently their performance, depends dramatically on the solidification process [5]. It is essential to understand the nucleation, grain growth, defect formation, and microstructural evolution during solidification to obtain the desired properties of metals.

Direct observation of the solidification process of metals is challenging as melts are opaque and the solidification usually happens at high temperatures [6]. The lack of advanced real-time techniques has limited previous studies investigating the relationship between the solidification parameters and resulting microstructure to postmortem analysis of the final microstructure and/or theoretical simulations [7−10] without the capability of providing a continuous, dynamic, and accurate description of the metal solidification process. Although some researchers have successfully observed the structural evolution of transparent organic solvents [11−15], these results can be hardly applied to the solidification of metals because of the large differences in the thermophysical properties between organic materials and metals.

Recently, the emergence of X-ray imaging techniques, especially synchrotron radiography and tomography, has provided the capability to monitor

*Wen-quan LU and Nai-fang ZHANG contributed equally to this work
Corresponding author: Qiao-dan HU, Tel: +86-21-54744246, E-mail: qdhu@sjtu.edu.cn
DOI: 10.1016/S1003-6326(22)65959-4

the solidification process of metals in real time [16,17]. Combined with a solidification apparatus, synchrotron X-ray imaging enables the visualization of the microstructure evolution in metals during solidification. This can provide valuable information for tuning the properties of metals by manipulating the solidification parameters. Here, we outline recent developments of the solidification apparatuses, including the directional solidification device, resistance furnace, multifield coupling device, semisolid forming device, aerodynamic levitation (ADL) apparatus, and laser additive manufacturing (LAM) apparatus. We mainly focus on the application of these apparatuses to the in situ characterization of the microstructure evolution during solidification via the synchrotron radiation X-ray imaging technique (Fig. 1).

2 Synchrotron radiation X-ray imaging

2.1 Synchrotron radiation

Synchrotron radiation is an electromagnetic radiation that originates from the tangent direction of the trajectory of charged particles with a velocity close to the speed of light [18]. Thus far, three generations of synchrotron radiation light sources have been developed [19], and the fourth generation is soon to be implemented. Synchrotron radiation X-ray sources have following characteristics [18]: (1) broad and continuous spectrum, (2) high degree of polarization, (3) collimation, (4) high brightness, (5) pulse time structure, (6) clean light source, and (7) computability. In recent years, synchrotron radiation X-ray imaging has been introduced to study the solidification process of metals using 2-dimension (2D), dynamic 2-dimension (2D plus time), 3-dimensional (3D), and 4D (3D plus time) methods. This technique enables to reveal the evolution of crystal nucleation and growth behavior during solidification [20−23].

2.2 Imaging mechanisms

As X rays exhibit wave–particle duality, both their amplitude and phase will change when they penetrate through an object. The interaction between materials and X rays can be described in terms of the complex refractive index (n) to [24]:

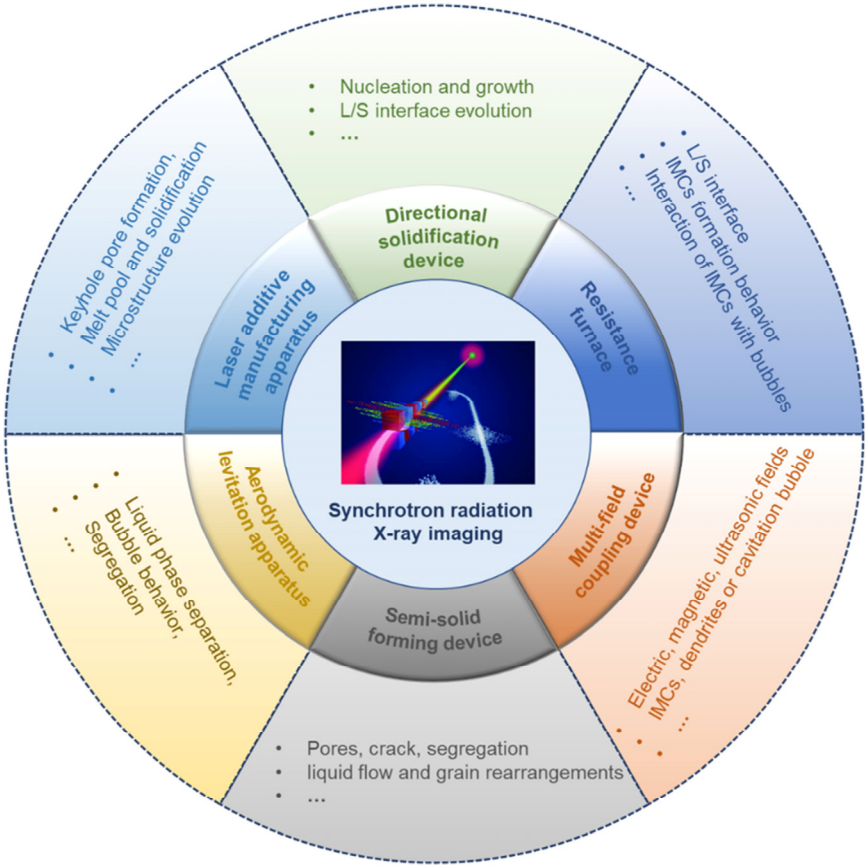

Fig. 1 Sketch of in situ characterization apparatus and research content during metal solidification process by synchrotron radiation X-ray imaging technique

$$n=1-\delta+i\beta \quad (1)$$

where δ is the absorption factor, and β is the phase factor. From Eq. (1), it can be seen that the complex refractive index allows for two different imaging mechanisms: the absorption factor permits absorption-contrast imaging, while the phase factor permits phase-contrast imaging. Therefore, the X-ray imaging technique mainly involves absorption-contrast imaging and phase-contrast imaging. Traditional X-ray imaging techniques based on absorption contrast have been widely used in clinical studies, materials science, and biology fields. However, absorption-contrast imaging mainly depends on the difference in the X-ray absorption capacity for different materials. Therefore, it is difficult to differentiate the light elements in biological soft tissue, fiber, and polymer materials. On the other hand, X-ray phase-contrast imaging effectively overcomes the shortcomings of traditional absorption imaging. After years of research, four phase-contrast imaging methods have been proposed: interferometry [25], the diffraction-enhancement method [26], the grating imaging [27], and the in-line phase-contrast imaging [28]. In fact, most of the presented X-ray imaging studies on metal solidification are based on absorption imaging mode, which always obtain a good image contrast.

3 Application of synchrotron radiation X-ray imaging to observe solidification processes

The design and manufacturing of the solidification equipment, including the directional solidification device, resistance furnace, multifield coupling device, semisolid forming device, ADL apparatus, and LAM apparatus, have progressed greatly. Through the combination of these solidification apparatuses, a series of advances have been made on the in situ observation of the metal solidification process via synchrotron radiation X-ray imaging. Here, we outline the latest advances on the application of synchrotron radiation X-ray imaging to the observation of the solidification process.

3.1 Directional solidification device

Figure 2 shows the sketch of a Bridgman directional solidification device [29]. There are two heating zones in the furnace, which are vertically distributed, and different temperature fields can be obtained by adjusting the temperature of each zone. At the same time, the sample holder inside the furnace is connected with a single-axis displacement controller, which can be used to adjust the pulling rate of the metal directional solidification. Bridgman directional solidification device can achieve stable control by adjusting the pulling rate (V) and the temperature gradient (G_L) at the front of a liquid–solid interface. There are two main ways to perform directional solidification experiments, pulling the sample at a velocity V in a static temperature field, and cooling the heaters at a rate R with the sample at rest ($R=G_LV$). The latter is the most used method at synchrotron radiation facilities since it facilitates imaging process. Up to now, combining this device with the synchrotron X-ray imaging technique, researchers have conducted in situ observations of various solidification behaviors during alloy directional solidification, such as dendrite coarsening [30−32], dendritic fragmentation and detachment [33−38], columnar-to-equiaxed transition (CET) [22,39−43], temperature gradient zone melting (TGZM) [21,44], and solid−liquid interface evolution [23,45−47].

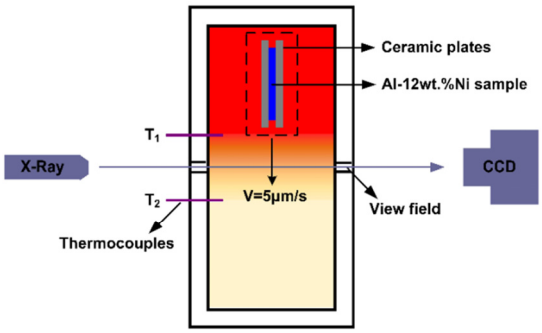

Fig. 2 Schematic diagram of Bridgman furnace [29]

3.1.1 Dendrite coarsening, fragment, and detachment

To reveal the dendritic growth behavior, LI et al [30,31] used the synchrotron X-ray imaging technique to observe the solidification process of a Sn–Bi alloy in real time, and they directly observed the dendrite coarsening process caused by dendrite remelting and merging between neighboring arms. The rates of dendrite remelting and coalescence as well as the evolution of secondary dendrite arm spacing (DAS) were measured from the captured

real-time images. It was found that the reason for dendrite coarsening in the early stage is dendrite remelting from the tips toward the roots.

YASUDA et al [33,34] observed the fragmentation of dendrite arms and their subsequent detachment under directional solidification of a Sn−Bi alloy at Spring-8. It was pointed out that both the local melt flow and the deceleration of dendrite growth rate are key factors for fragmentation. The in situ observations show that the detached crystals can grow into a stray crystal before the original dendrite tips are reached. In other words, the detachment of fragmented crystals is also a source of stray crystal formation. Similarly, MATHIESEN et al [22], RUVALCABA et al [35], and ARNBERG and MATHIESEN [36] observed the dendritic fragmentation caused by local solute-enrichment during the directional solidification of an Al−20wt.%Cu alloy. Figure 3 shows solute-enrichment during the fragmentation of the first tertiary dendrite arm selected from the 2D X-radiographic projection images. It can be seen that copper in the liquid around the fragment becomes enriched as solidification proceeds. The analysis suggests that the tertiary dendrite arms are more easily exposed to the incoming gravity-induced liquid flow. Both the solute carried by the liquid flow and the solute locally rejected lead to solute accumulation at the roots, which results in remelting and further detachment.

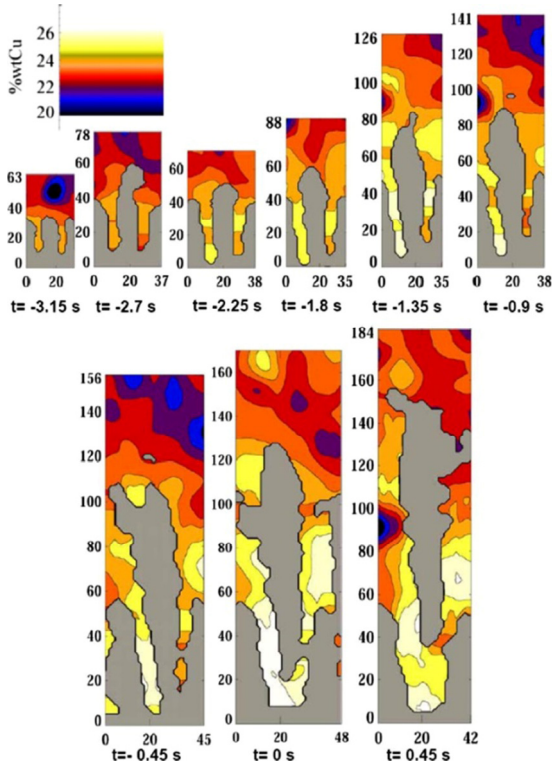

Fig. 3 Contours showing solute-enrichment during fragmentation of first tertiary dendrite arm (The Cu level coloring is indicated explicitly, and the masked-off solid has been colored in grey) [35]

3.1.2 CET

Dendrite fragments can promote the formation of equiaxed grains at the end of the columnar grains. To understand the transition mechanisms, RUVALCABA et al [35] and MATHIESEN et al [22] conducted in situ studies on the directional solidification of an Al−20wt.%Cu alloy and observed the CET under normal nonforced-convection conditions. It was found that the first fragment continues to grow dendritically and is transported toward the columnar front under the action of buoyancy, which causes further solute enrichment in the liquid left behind; as a result, the second fragment develops. Accordingly, a series of new fragments are released in the wake of the first one. This mechanism can effectively induce CET transformations during solidification. NGUYEN-THI et al [40] carried out an in situ characterization of the CET induced by a velocity jump in refined Al−3.5wt.%Ni alloys. As shown in Fig. 4, when a

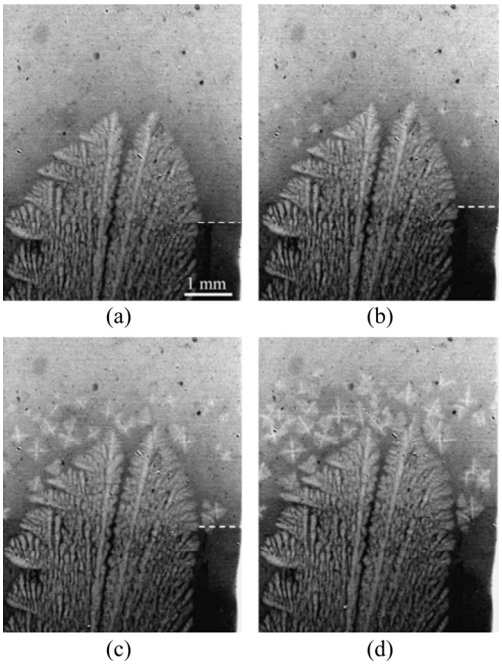

Fig. 4 Synchrotron radiation images of columnar-equiaxed transition induced by a sharp increase of growth velocity from 2 to 14 μm/s at $t=t_0$, during directional solidification of Al−3.5wt.%Ni alloy (Al appears in gray, while the Ni-enriched liquid is dark) [40]: (a) $t=t_0$+42 s; (b) $t=t_0$+63 s; (c) $t=t_0$+87 s; (d) $t=t_0$+111 s

low pulling rate (growth velocity V_g=2 μm/s) is applied, a dendritic columnar microstructure is obtained. When a velocity jump occurs, the CET is induced, and equiaxed grains appear within the dark Ni-enriched liquid layer surrounding the columnar structure. Subsequently, DONG et al [41] and LI et al [42] used the synchrotron radiation imaging technique to track and record the CET process induced by controlling the cooling rate of an Al−15wt.%Cu alloy. This study found that the density difference between the solid and liquid phases contributes to dendrite detachment, fragment transportation, and CET transformations.

3.1.3 Solid–liquid interface evolution

BOGNO et al [23,45] revealed the effect of melt convection on the solid−liquid interface shape during directional solidification of an Al−4wt.%Cu alloy via synchrotron radiography. As shown in Fig. 5(a), solute enrichment caused by melt convection can change the solid–liquid interface shape. Similarly, YASUDA et al [46] also directly observed the evolution of the solid−liquid interface

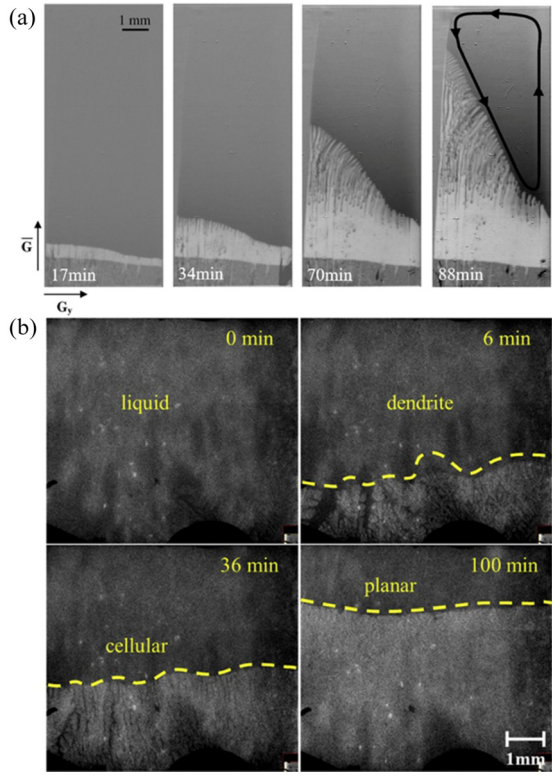

Fig. 5 Synchrotron radiation images of increasing macroscopic deformation of solid−liquid interface during initial transient of directional solidification of Al−4wt.%Cu alloy [23] (a) and overall observation of solid−liquid interface transition during directional solidification of sheet-like sample [48] (b)

in pure Fe. REINHART et al [47] attributed the formation of convex solid−liquid interface to the transversal temperature gradient, and found that the effect of solute flow on dendrites growth is different at different cooling rates. DONG et al [48] conducted in situ observations of the solid–liquid interfacial morphology transition during directional solidification of an Al–Zn alloy via X-ray imaging. From Fig. 5(b), it can be observed that, as the temperature gradient (G) increases, the solid−liquid interface morphology in sheet-like samples undergoes a significant transition from dendritic to cellular and finally to planar growth. They also found that the evolution of the solid−liquid interface morphology in sheet-like samples and 3D cylindrical samples under the same thermal conditions seems to be different. Planar growth appears more easily in the former than the latter because of the higher solid–liquid interface stability and the restricted liquid flow in 2D thin-plate samples.

3.2 Resistance furnace

The resistance furnace is one of the most commonly used heating apparatuses in industrial and scientific research fields. Indeed, the heating mode of some furnaces described in Section 3.1 is resistance heating. In order to differentiate between the resistance furnace and the directional solidification device, just in situ characterization of the microstructure evolution during isothermal heating and cooling is discussed in this section. Recently, combining the resistance heating apparatus with the synchrotron X-ray imaging technique, some researchers studied the crystal nucleation behavior and growth kinetics of intermetallic compounds (IMCs) during isothermal heating and cooling, mainly including the grain refining effect, growth of equiaxed grains, morphology evolution of dendrites, diverse morphologies and growth kinetics of multiphase IMCs, etc.

3.2.1 Crystal nucleation and growth behavior

The crystallization processes of metallic materials mainly include nucleation and growth. Understanding the nucleation process is of importance for being able to actively tune the final microstructure.

As the size of the crystals under formation is very small, it is hard to directly observe the

dynamic details of the crystal nucleation behavior using the synchrotron X-ray imaging technique. Additionally, manual counting methods cannot process the huge amount of X-ray radiography images effectively and accurately. In order to solve the above-mentioned problems, LIOTTI et al [49] investigated the crystallization process during solidification of an Al–Cu alloy (near isothermal, and the temperature gradient is smaller than 1 K/mm) under different cooling rates via synchrotron radiography combined with machine learning. They analyzed a huge number of radiographic images using a computer vision algorithm to automatize the measurement of the number of crystals and nucleation undercooling (Fig. 6). Specifically, for each detected crystal, they estimated the nucleation position and time according to the growth rate. After measuring the liquid composition at the nucleation position, the local temperature can be obtained from the phase diagram. Then, nucleation undercooling was calculated, and the nucleation undercooling distribution was found to be consistent with the free growth model of nucleation. They also revealed the relationship between nucleation bursts and the solute-suppressed zone during solidification. Their work demonstrates that machine learning permits a better understanding of the solidification microstructure evolution and is beneficial to the verification and improvement of the solidification theory.

To reveal the heterogeneous nucleation behavior, JIA et al [50,51] investigated the heterogeneous nucleation process of a solidifying Al–Cu alloy inoculated by Al–Ti–B via synchrotron radiography. They obtained the solute concentration profile and found that a suppressed nucleation zone (SSNZ) exists during solidification. The final grain size mainly depends on the size of this SSNZ and the distribution of the activated nucleants. They also quantified the effects of the Zr addition on the grain size and clarified the Zr poisoning mechanism [52]. XU et al [53] also quantified the nucleation rate and dendrite growth rate of a hypoeutectic Al–Si alloy with different refiners using synchrotron radiography and revealed the refinement mechanism of (Ti,Nb)B_2 for epitaxial nucleation and free growth. They found that the Al−1.67Ti−3.33Nb−0.5B alloy provides a higher nucleation rate and a lower dendrite growth rate than the Al−5Ti−B alloy. Furthermore, the (Ti,Nb)B_2 particles are more resistant to silicon toxicity than the TiB_2 particles. The number density of the (Ti,Nb)B_2 particles can also significantly affect grain refinement.

After nucleation, the crystals gradually grow in various forms during solidification. Using synchrotron radiography, BOGNO et al [54] observed the growth and interaction of equiaxed grains in Al−10wt.%Cu alloy. The equiaxed solidification achieved in almost isothermal conditions was continuously monitored, and it was found that equiaxed dendrite growth appears in two growth modes. The accelerating growth mode corresponded to the early stage of dendrite growth, and the decelerating growth regime was attributed

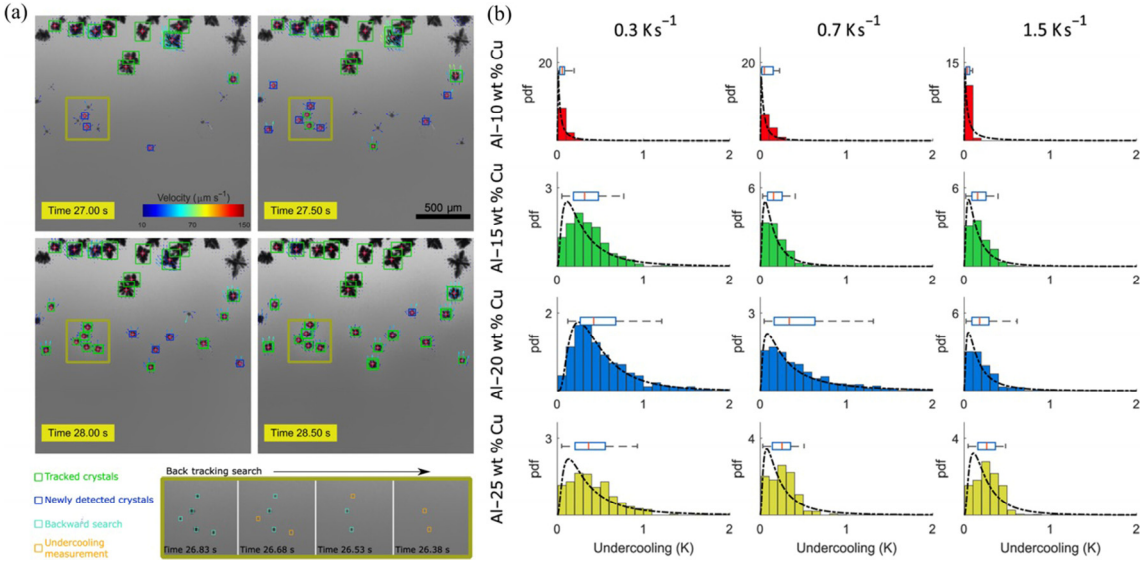

Fig. 6 Nucleation undercooling measurement method (a) and nucleation undercooling distributions (b) [49]

to the overlap of solute diffusion field in front of the advancing dendrite tips in the later growth stage. YASUDA et al [55] found that δ phase change to γ phase occurs when the cooling rate is larger than 0.33 K/s, and the γ phase prefers to nucleate in a favorable plane of δ phase during solidification of Fe−C alloys. GIBBS et al [56] characterized the dendritic growth in an Al−24wt.%Cu alloy through X-ray tomographic technique. Based on the measurements of the evolution of the volume fraction, the surface area per unit volume, and the interface shape distributions of solid phase, the authors found that the growth of the dendrite structure is lack of self-similarity. Using 4D (3D plus time) imaging technique, AZEEM et al [57] direct observed the dendritic growth process in solidifying Ni, Fe and Co alloys with the cooling rate of 0.05 K/s. From Fig. 7, for Ni alloys, the grains first nucleate on the sample surface, then form dendrites with branched secondary and tertiary arms, and finally form interlock mesh structure. For Fe alloys, the Fe dendrites appear coarsening at the later stage of solidification. For Co alloys, competitive growth between dendritic arms of the same grain occurs during solidification.

3.2.2 IMC formation and interaction with bubbles

IMCs and hydrogen bubbles are common in metal alloys. Through in situ synchrotron radiography, YU et al [58] directly observed the intermetallic evolution during solidification of an Al−10Si−0.3Fe alloy and revealed the formation mechanism of the intermetallic δ phase. It was shown that, independent δ plates first nucleate and grow, while, subsequently, they block each other, and eventually, δ plates always form branched configurations. FENG et al [59] investigated Fe-rich IMC formation under TiB_2 and TiC inoculation. They found that TiB_2 and TiC inoculation can increase the formation of Fe-rich IMCs, and the formation rate and number of IMCs are the highest under near-isothermal solidification.

Hydrogen pores originate from hydrogen absorption and hydrogen release during the preparation process. Trapped hydrogen pores after solidification can deteriorate the mechanical properties of castings [60]. Therefore, it is necessary to investigate the bubble behavior and the influence

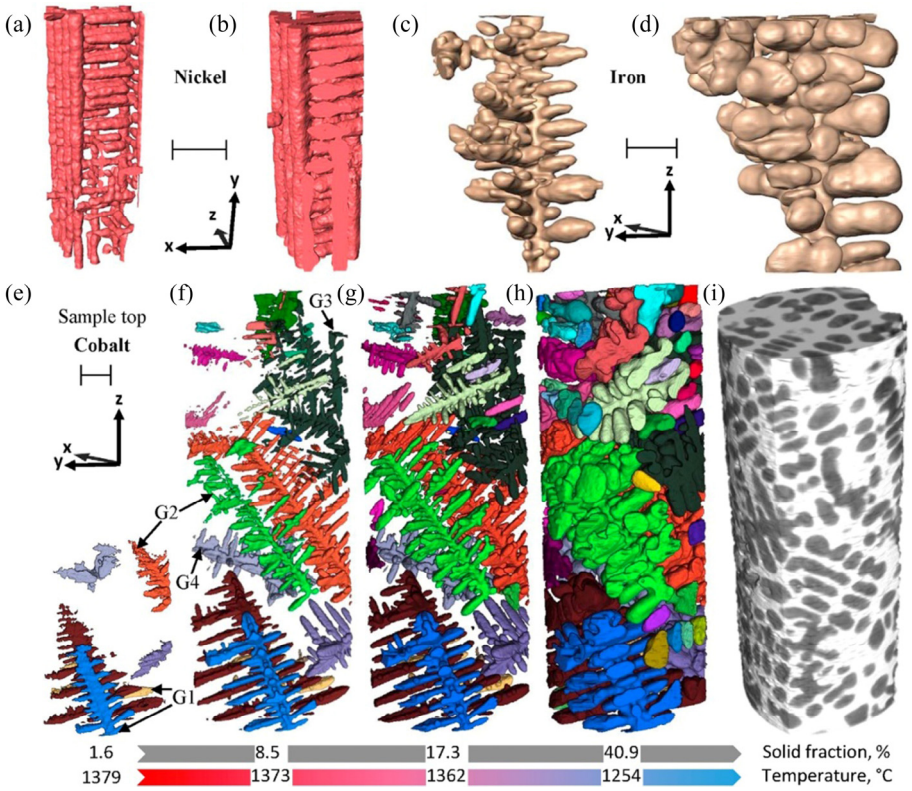

Fig. 7 3D evolution of dendritic patterns in Ni−14wt.%Hf, Fe−11wt.%Hf and Co−18wt.%Hf alloys during solidification at cooling rate of 0.05 K/s [57]: (a, b) FCC α-Ni dendritic patterns at 495 s and 1496 s after start of solidification; (c, d) Development of single δ-Fe pattern during solidification at 396 s and 3960 s; (e−h) Development of α-Co patterns during solidification of Co alloy; (i) Raw data of reconstructed volume corresponding to (h)

of bubbles on the microstructure evolution, especially regarding the formation and growth kinetics of IMCs. The bubble growth and IMC dissolution behavior as well as their interaction were investigated in melting Al−Mn alloys. LU et al [61] directly observed that the pores varied gradually from being irregular to subglobose and finally assumed a spherical shape with increasing temperature. The variation in bubble volume changed the IMC dissolution rate, and the IMCs around the bubbles completely dissolved into a matrix melt before those that were located at a distance from the bubbles. The impact degree of IMC dissolution on bubble growth was found to be smaller than that on the collapse of surrounding bubbles. Particularly, it was found that new IMCs appeared during the heating process because of the fluctuations in the Mn solute concentration caused by bubble coalescence upon heating an Al−10wt.%Mn alloy. Furthermore, the coalesced bubble could push the newly-formed IMCs to move (Fig. 8). A formula describing the supersaturation fluctuation during the bubble coagulation process was developed [62].

3.2.3 Formation sequence and growth of IMCs at liquid–solid interface

Metallurgical bonding between dissimilar metals at high temperature is often accompanied by the IMCs formation. And the formation and growth of the IMCs at the interface are key parameters for controlling the microstructure and properties. Synchrotron radiography has been proven to be an effective approach for investigating in situ the formation sequence of IMCs at the liquid–solid interface, which is helpful for understanding the interfacial reaction process accurately and clearly [63−70]. MOHD SALLEH et al [64] performed in situ observations of the reaction at the solid Cu–liquid Sn interface using the synchrotron X-ray imaging technique (Fig. 9). The dynamic experimental results showed that, upon molten solder wetting and the rapid dissolution of Cu near the solid–liquid interface, an instant planar Cu_6Sn_5 layer with considerable thickness was first formed, followed by the formation of subsequent scallop-shaped Cu_6Sn_5 IMCs during heating. Through in situ observations, DING et al [66,67] studied the formation sequence of IMCs at the Al−Ni liquid−solid interface under different saturation conditions in the melt. It was found that the formation time of Al−Ni IMCs was closely related to the degree of saturation in the melt. When Ni in the melt at the liquid–solid interface was supersaturated, Al_3Ni_2 was formed first followed by Al_3Ni, as shown in Fig. 10(a) [66]. When Ni in the melt was unsaturated, layered Al_3Ni_2, peritectic Al_3Ni, and proeutectic Al_3Ni IMCs were formed sequentially during cooling (Fig. 10(b)) [67]. Al_3Ni_2 layer growth was mainly controlled by the diffusion mechanism and can be divided into four stages (Fig. 10(c)) [68], the similar results were also obtained in their another study on the growth process of η layer formed at the liquid Al–solid Fe interface, and η was the preferred phase generated during holding time [68].

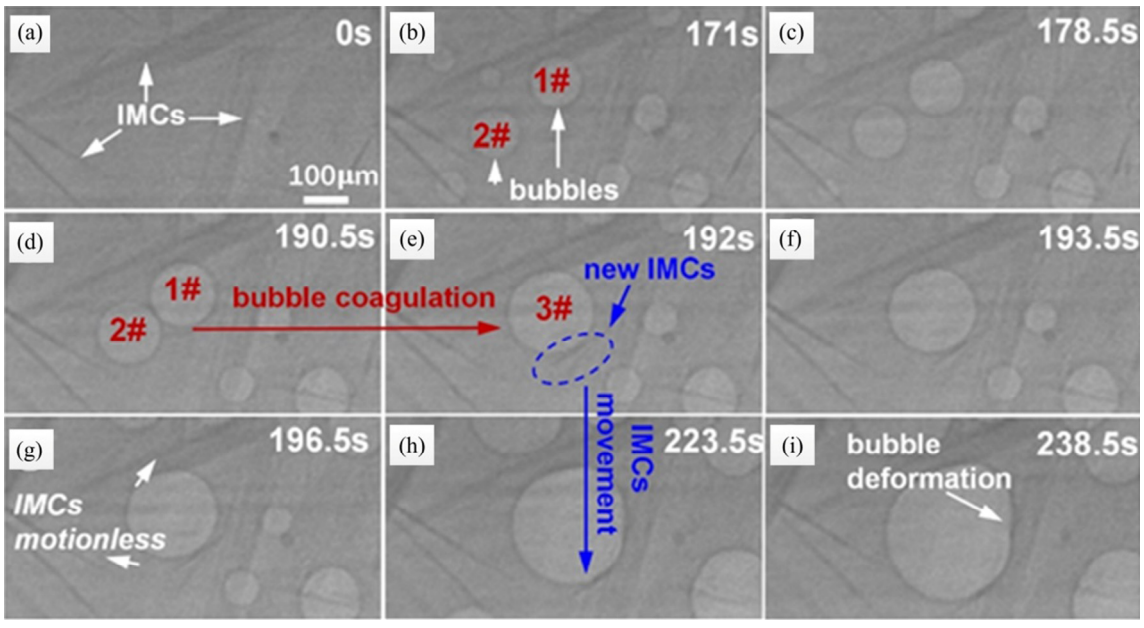

Fig. 8 Microstructure evolution during heating of Al−10wt.%Mn alloy with heating rate of 0.7 K/s [62]

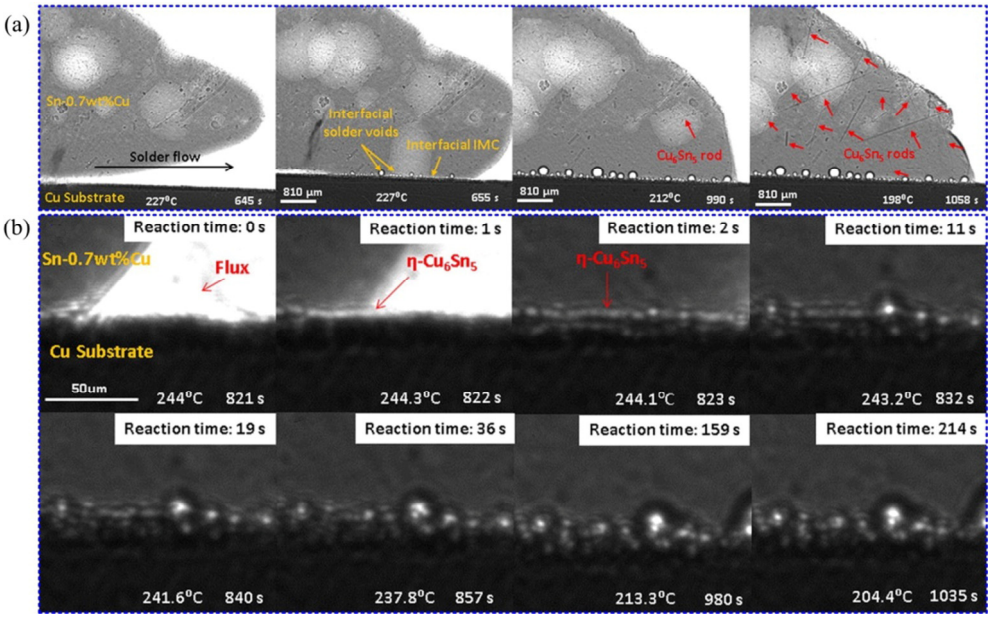

Fig. 9 In situ real-time imaging observations of reactions between Sn−0.7wt.%Cu and Cu substrate interface (a) and high-magnification in situ real-time imaging observations of IMC formation between Sn−0.7wt.%Cu and Cu substrate interface (b) [64]

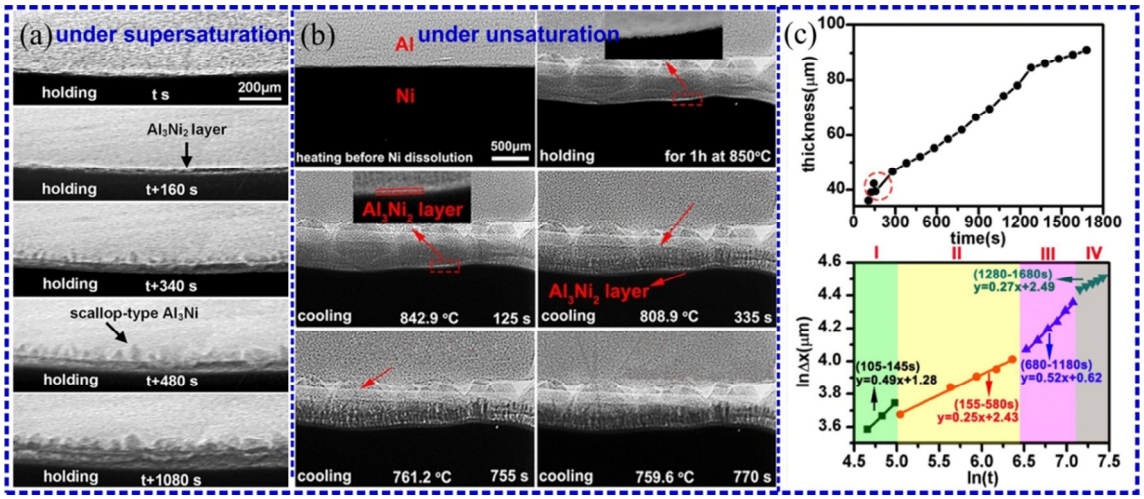

Fig. 10 Synchrotron radiation images of microstructural evolution at liquid Al and solid Ni interface under super-saturation [66] (a); in situ images of interfacial microstructures under unsaturation [67] (b); time dependence of Al_3Ni_2 layer thickness [67] (c)

Similarly, Al−Cu IMCs formed at the Al−Cu bimetal interface are also complex. WANG et al [69] direct observed various interfacial transition zones with different X-ray contrasts around the Al–Cu bimetal interface. These interfacial transition zones were identified to be α(Al) dendrites, (α(Al)+Al_2Cu) eutectic structures, the Al_2Cu IMC, and the ($AlCu+Al_3Cu_4+Al_2Cu_3$) IMC layer (Fig. 11(a)). Then, the formation sequence and multiphase growth kinetics of the diversified IMCs at the Al−Cu liquid–solid interface were dynamically observed by DING et al [70]. They found that chemical reaction dominates the growth of γ_1 layer, and the limited atoms diffusion can lead to the growth deviations of primary ε_2 and tertiary β from original linear relationship. In addition, the difference in critical thickness between the growing IMCs and new IMCs was mainly related to the ratio of their solute concentration range, a larger ratio of solute concentration range between the later formed IMC and the growing IMC preferred an increasing critical thickness of the growing phase, as shown by the schematic diagram in Fig. 11(b).

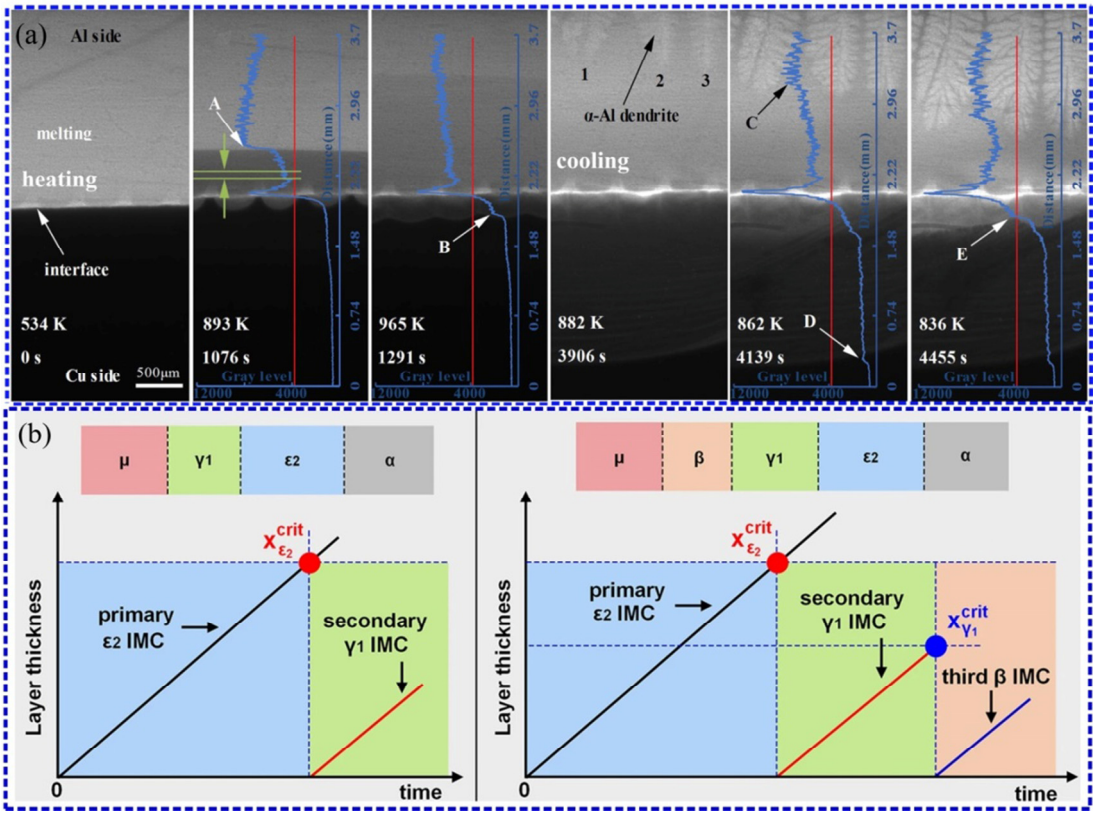

Fig. 11 Sequence of in situ radiographs showing diffusion behavior around interface during melting and solidification of Al/Cu bimetal [69] (a); schematic diagram showing primary ε_2 layer reaching its critical thickness followed by secondary γ_1 IMC formation and secondary γ_1 IMC layer reaching its critical thickness followed by tertiary β IMC formation [70] (b)

3.2.4 Diverse morphologies of IMCs at liquid−solid interface

IMCs can exhibit both facet and nonfacet growth characteristic, which reflects the diversity of their growth morphology. The diverse morphologies of IMCs during melting and solidification at the liquid–solid interface have been studied using synchrotron radiography [66,71−78]. DING et al [66] observed the diversified morphology and growth behavior of the Al_3Ni phase at the liquid Al–solid Ni interface by controlling the saturation in the molten layer. Scallop-type and columnar Al_3Ni were obtained in the diffusion couples with supersaturated and unsaturated melt layers, respectively (Figs. 12(a, b)). The growth of columnar Al_3Ni grain is often accompanied by the dissolution of adjacent small columnar grains (Fig. 12(c)). For the scallop-type Al_3Ni formed during holding (Fig. 12(e)), the growth is mainly governed by the annexation of adjacent small grains, leading to its morphology changing from scallop-like to hemisphere-like.

For the proeutectic Al_3Ni phase formed at the liquid Al–solid Ni interface during solidification, the morphology is diversified. According to the 2D and 3D studies of proeutectic Al_3Ni with synchrotron radiation X-ray imaging [73,74], the typical morphologies are mainly prisms with faceted growth behavior and complicated dendrites with asymmetrically distributed arms, as shown in Fig. 13. The former mostly consists of a hollow quadrangular prism, which is usually formed at a slower cooling rate, while the latter is formed at a faster cooling rate. They also found that the growth of prismatic Al_3Ni is anisotropic with preferential and rapid growth occurring along the [001] direction, and hollows appear in the solid phase after a certain growth time. Faceted V-shaped grooves are also observed at the distal end of some dendrites, which is considered to be the evidence that the transition from the faceted to the dendritic morphology does not take place suddenly.

ZHANG et al [78] used the synchrotron X-ray imaging technology to study the effect of Si on the

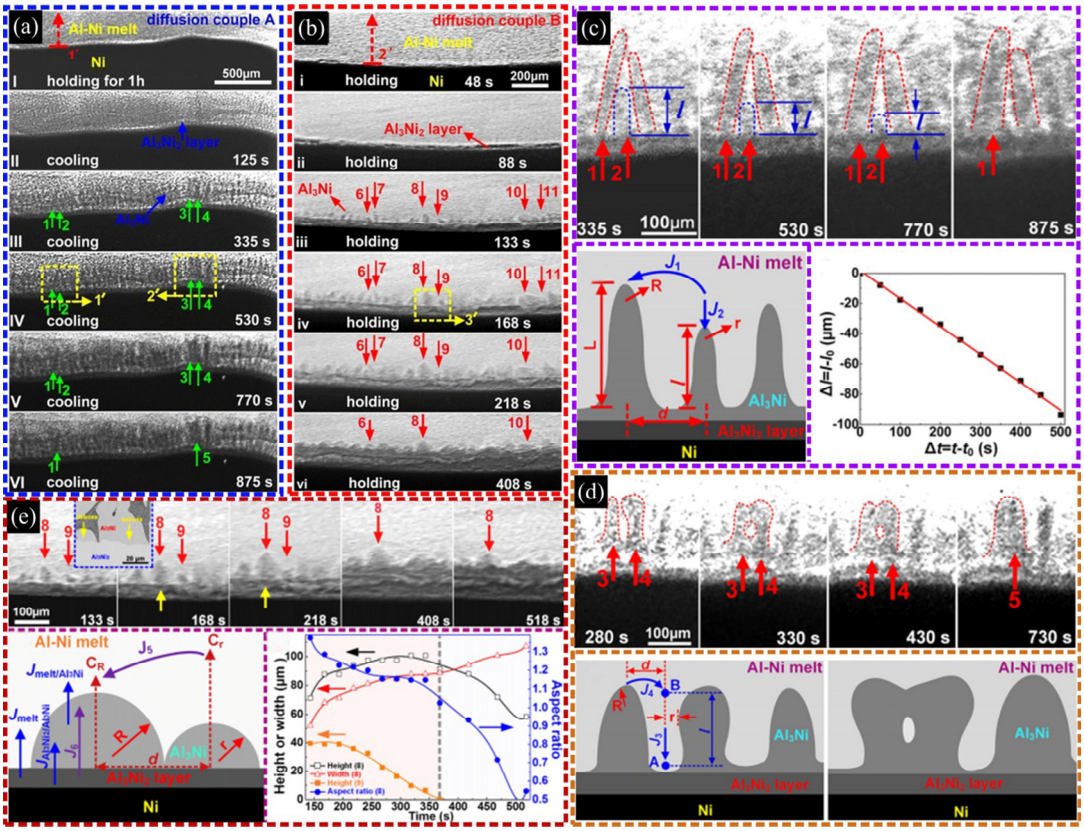

Fig. 12 In-situ real-time growth of Al_3Ni phase for diffusion couples with different saturation in melt layer (a, b); synchrotron radiation images and schematic diagram of growth of Al_3Ni grains extracted from yellow dashed box 1 (c), 2 (d) and 3 (e) in (a) [66]

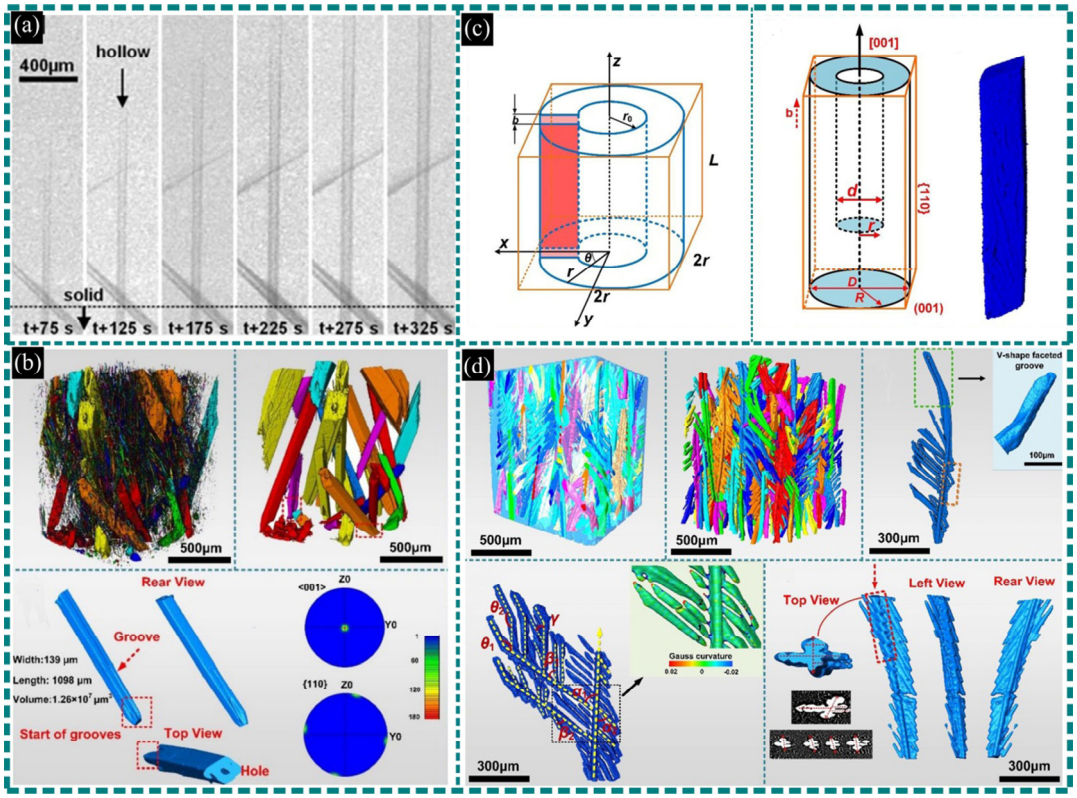

Fig. 13 In situ images of hollowed proeutectic Al_3Ni crystals [73] (a); 3D morphology of hollowed proeutectic Al_3Ni crystals [74] (b); schematic of screw dislocation and formation mechanism of proeutectic Al_3Ni hollow prism [74] (c); 3D morphology of dendritic proeutectic Al_3Ni [74] (d)

growth behavior of the Fe_2Al_5 phase at the Al–*x*Si (liquid)–Fe (solid) interface during holding. It was observed that the addition of Si to the melt caused a significant change in the morphology of Fe_2Al_5 phase. For the Al/Fe diffusion couple, Fe_2Al_5 presented an irregular morphology with a fast growth toward the solid Fe substrate. During growth, the Fe_2Al_5 crystal roots near the melt side merged into a layered shape, but the growth tip always maintained a tongue-like appearance. By comparison, in the Al–*x*Si/Fe diffusion couples, the tongue-like morphology was completely replaced by the layered morphology with a planar growth front. The dissolution rate of the layered Fe_2Al_5 phase was significantly lower than that of the tongue-like Fe_2Al_5 during the early holding stage, but in the final stage, the dissolution rates of layered Fe_2Al_5 and tongue-like Fe_2Al_5 tended to be similar.

3.3 Multifield coupling device

Application of external physical fields is an effective method to tune the microstructure by affecting the nucleation and growth during solidification. At present, many researchers have used the synchrotron radiation X-ray imaging technique to investigate the influence of electric fields [79−86], magnetic fields [87−91], ultrasonic field [92−102] on metal solidification. These works provide a better understanding of the effect of external fields on the solidification behavior.

3.3.1 Effects of electric field on solidification behavior

WANG et al [79,81] observed the morphological evolution of dendrites during the solidification of Sn–Bi alloys under direct-current (DC) and pulsed-current electric fields. The schematic diagram of the experimental setup with an electric field at the Shanghai synchrotron radiation source is shown in Fig. 14. They found that, upon a DC electric field, dendrites had the tendency to transform from columnar crystals to equiaxed crystals, and the growth of sharp dendrite tips was noticeably suppressed. The primary and secondary arms tended to be shorter and thicker, while the growth of the tertiary arms was completely inhibited, and tertiary arms disappeared eventually. In this work, the morphological evolution of the dendrites was attributed to the Joule heating effect and the current crowding effect, which caused a preferential accumulation of heat at the tip of the dendrites. In addition, when a pulsed-current electric field was applied during the whole solidification process, the start of solidification was delayed, and the incubation time became longer. After undercooling was accumulated to a certain degree, more dendrites suddenly nucleated and then simultaneously grew into fine dendrites with narrow arm spacing (Fig. 15). The real-time results also indicate that a pulsed-current electric field has no obvious effect on crystal grain refinement when it is applied during crystal growth only.

Subsequently, using synchrotron radiation X-ray imaging technique, many researchers studied the solidification behavior of Sn-based alloys under the action of electric field. For example, YANG et al [83] found that the final grain size was sensitively dependent on the DC intensity in Sn−50wt.%Pb alloy. When the current density was smaller than a critical value, the grain size decreased with increasing DC density, while when the applied DC density exceeded the critical value, a coarser microstructure was obtained. WANG et al [84] observed the growth behavior of the Cu_6Sn_5 IMC during solidification of Sn−6.5Cu under an applied DC field. DC fields in the range

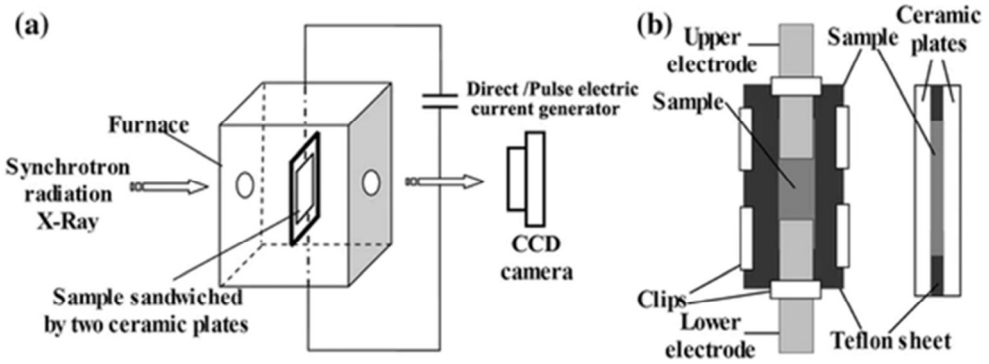

Fig. 14 Schematic diagram of experimental setup [81]: (a) Device configuration; (b) Sample with electrodes

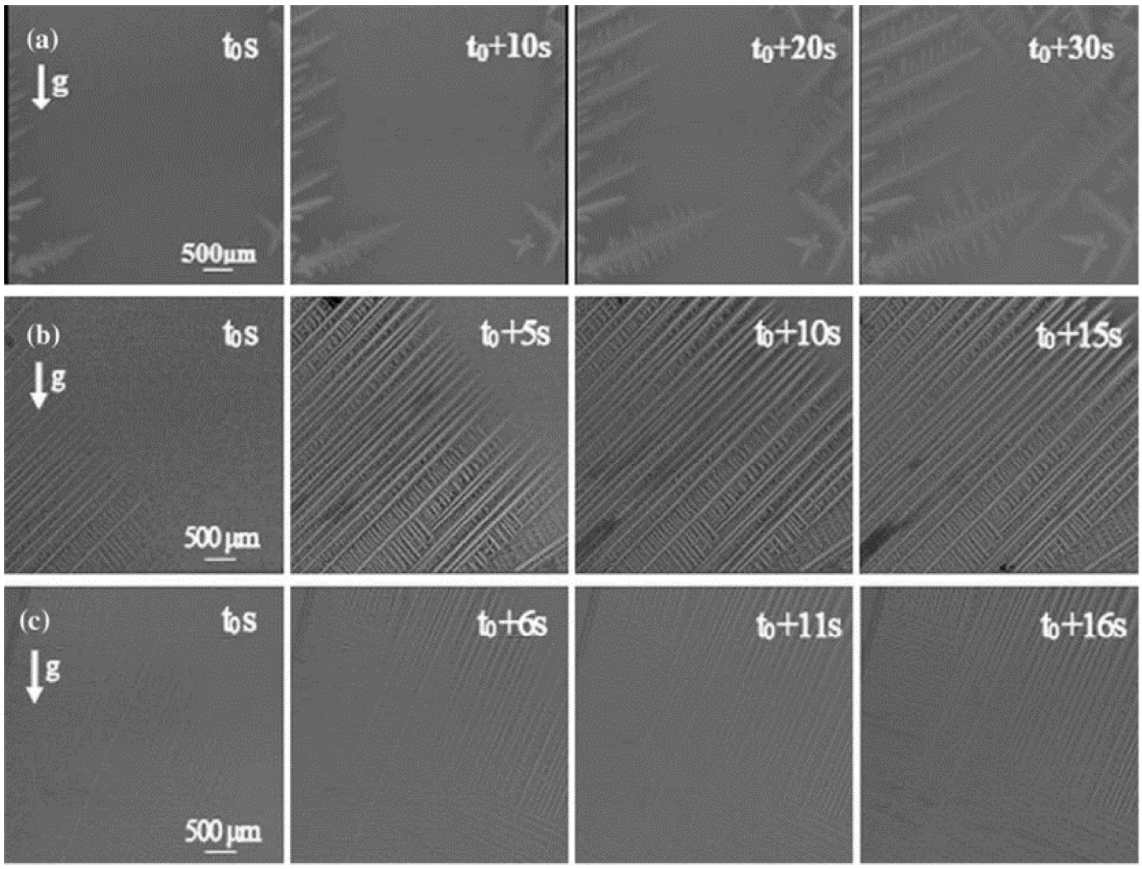

Fig. 15 Morphological evolution of dendrites in Sn−12wt.%Bi alloy [81]: (a) Without ECP; (b) ECP 1 with t=10 s, v=7 V; (c) ECP 2 with t=0.5 s, v=7 V

from 10 to 100 A/cm^2 had a pronounced contribution to the enhancement in both the growth rate and mean size of Cu_6Sn_5. Furthermore, the effect of the field with a DC of 10 A/cm^2 was more significant than that of the field with a DC of 100 A/cm^2. This was attributed to multiple factors, such as the diffusion rate, Joule heat, and potential barrier under the influence of the DC field. XUAN et al [86] studied the effect of a DC field on the morphological evolution of the primary phase Cu_3Sn and the peritectic phase Cu_6Sn_5 in a Sn−10wt.%Cu hyperperitectic alloy. It was found that the peritectic phase was directly precipitated from the matrix liquid phase instead of the peritectic reaction.

3.3.2 Effects of magnetic fields on solidification behavior

The influence of magnetic fields, including static magnetic field, traveling-wave magnetic field, and pulsed magnetic field, on the solidification of metals has received extensive attention. Using the synchrotron X-ray imaging technique, LIOTTI et al [87] developed an in situ technique to study the dendrite fragmentation behavior induced by a pulsed electromagnetic field (static magnetic field + pulsed current). Figure 16 shows the schematic of the sample arrangement and experimental setup. From Fig. 16, a permanent ring magnet is placed near the sample (at a distance of about 3 mm), and this magnet generates the static magnetic field with filed lines roughly perpendicular to the surface of the sample. Furthermore, a pulsed current is sent through the sample, producing a pulsed Lorentz

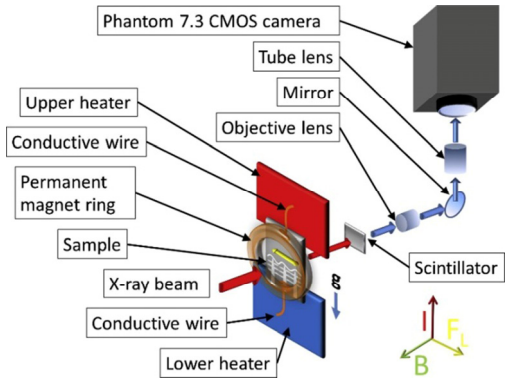

Fig. 16 Schematic of sample arrangement and experimental setting [87]

force that stirs the liquid. Figure 17 shows the image sequences and their fragmentation maps for the solidification process of an Al−15wt.%Cu alloy with or without a pulsed electromagnetic field, and it was found that the application of the pulsed electromagnetic field can lead to an increase in the dendrite fragmentation rate. The spatial distribution of the fragmentation events was similar, approximately even at the primary dendrite tips and the mushy zone. It was pointed out that the movement of the interdendritic liquid induced by the pulsed electromagnetic field was the main mechanism behind the observed increase in the fragmentation rate, through which the instability of the local temperature–concentration–curvature equilibrium and the remelting rate in the most vulnerable microregions were enhanced. In another work, LIOTTI et al [89] used the synchrotron radiation imaging technique to further study the influence of different solidification directions on the temporal and spatial distribution of dendrite fragmentation with an applied pulsed electromagnetic field (PEMF) and established a solute-driven remelting model to rationalize this influence.

CAO et al [90] used synchrotron radiography to investigate the solute distribution and dendritic growth in the unidirectional solidification of a Sn−50wt.%Pb alloy under a traveling magnetic field (TMF). It was found that, with the application of a TMF, a forced melt flow was induced from left to right, which promoted the redistribution of the solute in the interdendritic zone and affected the growth and morphology of the dendrites, including dendrites inclination, remelting, and fragmentation.

XU et al [91] characterized the 3D morphology of the micropores in directionally solidified Al−Cu alloys and studied the formation and morphology transition of these micropores under various TMFs. The results showed that the 3D morphology of the micropores was transformed from a dendrite structure to a relatively equiaxed structure with increasing magnetic flux density. On the other hand, the micropore volume fraction decreased. It was pointed out that the forced convection induced by the TMF broke the dendrites and promoted liquid feeding, leading to the decrease in porosity. In addition, only when the magnetic field was applied during nucleation or in the early growth stages, an effective void suppression could be achieved.

3.3.3 Effects of ultrasonic fields on solidification behavior

An in situ study of a metal melt under ultrasonic field based on synchrotron radiation imaging was carried out by LEE et al [92]. In this work, the dynamics of ultrasonic bubbles in a liquid Sn–Bi alloy with low melting point was captured in situ for the first time, thereby providing a more quantitative insight into the highly transient behavior of ultrasonic bubbles and their interaction with the surrounding liquid. In another work [93], LEE and coworkers studied the ultrasound cavitation in a Sn−Bi alloy and found that the microstructure evolved under application of ultrasonic waves. Furthermore, the oscillation and implosion of bubbles and the fracture process of a

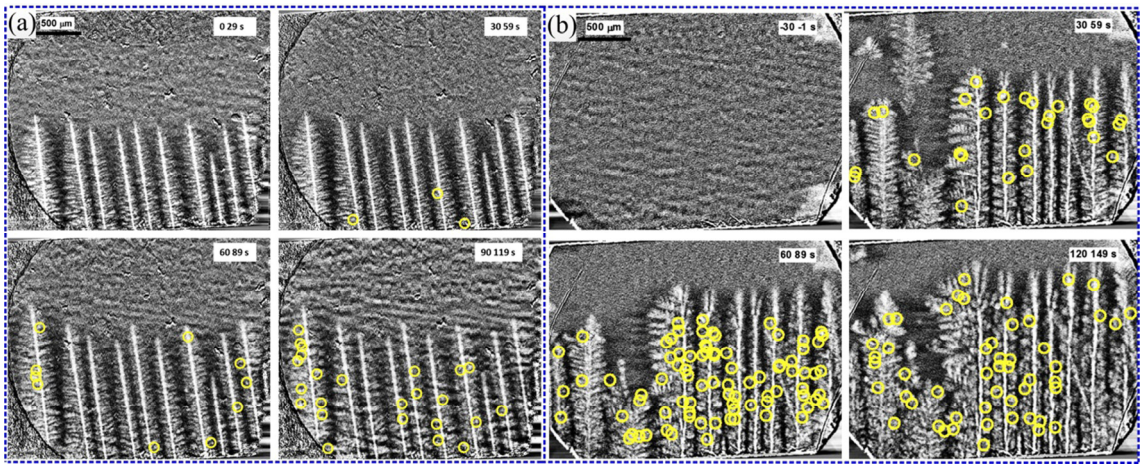

Fig. 17 Fragmentation maps from sequence during solidification of Al−15wt.%Cu: (a) No external PEMF; (b) With PEMF (In each image, the location of a fragmentation event within the 30 s time frame is identified by a yellow circle) [87]

secondary dendrite arm caused by a quasi-steady state bubble were clearly captured, which provided further in situ data for the quantitative understanding how ultrasonic waves influence dendritic growth and promote grain refinement.

HUANG et al [94] used the synchrotron radiation X-ray imaging technology to study the acoustic cavitation behavior during ultrasonic treatment of an Al−Cu alloy melt with high melting point. Figure 18 shows an accumulated image of a cavitation bubble that has undergone thousands of periods of ultrafast oscillations. The accumulation and oscillation of transient cavitation bubbles were captured, and the size distribution of the cavitation bubbles in the cavitation zone was quantitatively analyzed; it was found that it obeyed a truncated Gaussian distribution. TAN et al [95] studied in situ the dynamic behavior of ultrasound bubble implosion and the interaction between ultrasonic waves and semisolid phases during the solidification process of a Bi−Zn alloy. Real-time ultrafast X-ray imaging revealed that the ultrasonic bubbles in the liquid metal moved faster than the primary particles. At the same position close to the ultrasonic generator, the moving velocity of the bubbles was 70%−100% higher than that of the primary particles. The impact range of the shock wave generated by an ultrasonic bubble implosion was several times that of the original bubble diameter. The strong swirling flow formed instantaneously by ultrasound waves in the semisolid melt could effectively detach solid particles from the liquid–solid interface and redistribute them into the bulk of the liquid. XU et al [98] observed cavitation bubbles induced by an external ultrasonic field in a molten Al−10wt.%Cu alloy using in situ synchrotron X-ray radiography and quantitatively analyzed their size distribution, number density, and growth rate through the collected statistical data. The ultrasound cavitation and bubble dynamics were revealed.

Recently, some researchers have focused on exploring the fragmentation and refinement of solidifying phases in the solidifying melt under ultrasonic fields. WANG et al [99] studied in situ the effect of ultrasonic melt processing on preexisting primary Al_2Cu in a hypereutectic Al−Cu alloy using high-speed synchrotron X-ray radiography. It was found that ultrasonic melt processing has a significant effect on the fragmentation of preexisting primary Al_2Cu. The dynamic fragmentation processes of intermetallic Al_2Cu induced by ultrasonic melt processing are clearly captured. It was pointed out that the fragmentation of primary Al_2Cu intermetallic dendrites was induced by multiple mechanisms, such as cavitation bubble cloud, acoustic streaming flow, fragment collision, and pulsating cavitation bubbles during ultrasonic melt processing. ZHANG et al [102] utilized the in situ synchrotron X-ray imaging technology to study the dendrite fragmentation dynamics in a Al−15wt.%Cu alloy during solidification under the action of an ultrasonic field. A quantitative study was carried out on the 4D dendrite fragment distribution, morphology, and growth rate using ultrafast synchrotron X-ray tomography. This provided valuable 4D information for the optimization of ultrasound melt processing in industry.

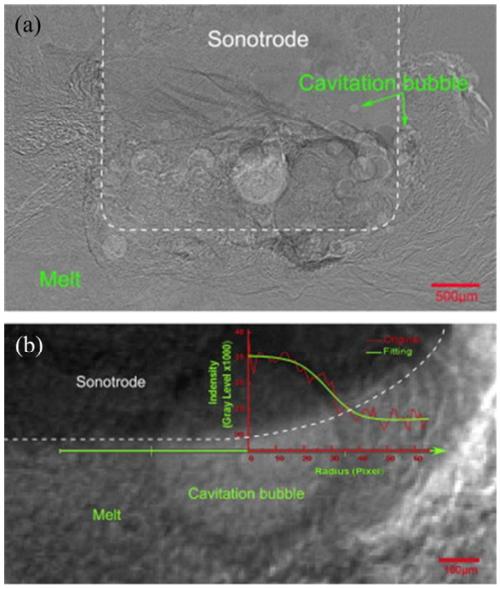

Fig. 18 X-ray imaged cavitation bubbles in Al−10wt.%Cu alloy melt (a), and light intensity distribution along centerline of X-ray imaged cavitation bubble (b) [94]

3.4 Semisolid forming device

Semisolid forming is a near-net forming technique for preparing alloys in the coexistence of solid and liquid phases. Since it was first proposed, this method has received much attention [103−108]. Compared with the traditional casting method, semisolid forming has many advantages, including high efficiency, short process duration, and being eco-friendly, etc. However, due to localization of strain under external loading and thermal expansion,

the produced parts have many defects, such as pores, hot cracks, and segregation. Therefore, to obtain products with a uniform structure and excellent performance, it is urgently needed to reveal the deformation mechanism of semisolid forming. Very recently, some researchers have investigated the semisolid deformation mechanism via the synchrotron X-ray imaging technique, including 2D, 3D, and 4D investigations [107−122]. Figure 19 shows the sketch of the semisolid compressive and tensile deformation apparatus together with synchrotron X-ray imaging [107,108]. From Fig. 19, regardless of the compressive or tensile devices, the semisolid deformation apparatus mainly includes two parts: the movable cell and the furnace.

3.4.1 Semisolid compressive deformation behavior

Using synchrotron radiography, FONSECA et al [109] investigated the granular shear deformation behavior and deformation-induced microstructural change in semisolid low-carbon steel. They revealed the microscopic behaviors of grain rearrangement, interstitial fluid flow and shear-induced expansion during the deformation process. GOURLAY et al [110] reported equiaxed-dendritic and globular microstructures in semisolid Al−15wt.%Cu alloys at different solid fractions, and they provided direct evidence of shear-induced dilation behavior. SU et al [111] studied the compression process in a semisolid Al−Cu alloy via synchrotron radiography and 2D-coupled lattice Boltzmann method–discrete element method (LBM−DEM) simulations. The complex deformation behaviors were simulated with good accuracy.

Using the synchrotron tomography, CAI et al [112,113] performed a quantification analysis of the granular and intragranular deformation behavior in a semisolid Al−15wt.%Cu alloy and uncovered the behaviors of liquid flow, crack nucleation and growth, dilation, grain deformation, and segregation formation. They found that void formation results from local expansion during the compression process, and they confirmed the three stages of pores evolution as follows: (1) shrinkage of the preexisting pores, (2) incubation stage, and (3) final rapid growth. They also observed the grain rotation and grain movement during extrusion, and the quantity of liquid extrudate increases with increasing displacement [107]. BHAGAVATH et al [114] also investigated bubble behavior during semisolid compression and subsequent solidification. It was found that pores nucleate in the liquid channels, grow consistently with the development of the liquid channels, and eventually form cracks. Further analysis showed that the behavior of bubbles in the compression and solidification stages was controlled by different mechanisms: (1) deformation-induced growth during the semisolid compression period, and (2) diffusion-controlled growth during subsequent solidification. KAREH et al [115] studied the preexisting pore behavior in Al−Cu alloys during semisolid compression. They found that the behavior of the preexisting pores varied with the solid fraction, and the main reason for pore opening was shear-induced dilation. In another work, they investigated discrete grain behavior and showed that shear-induced dilation was also responsible for

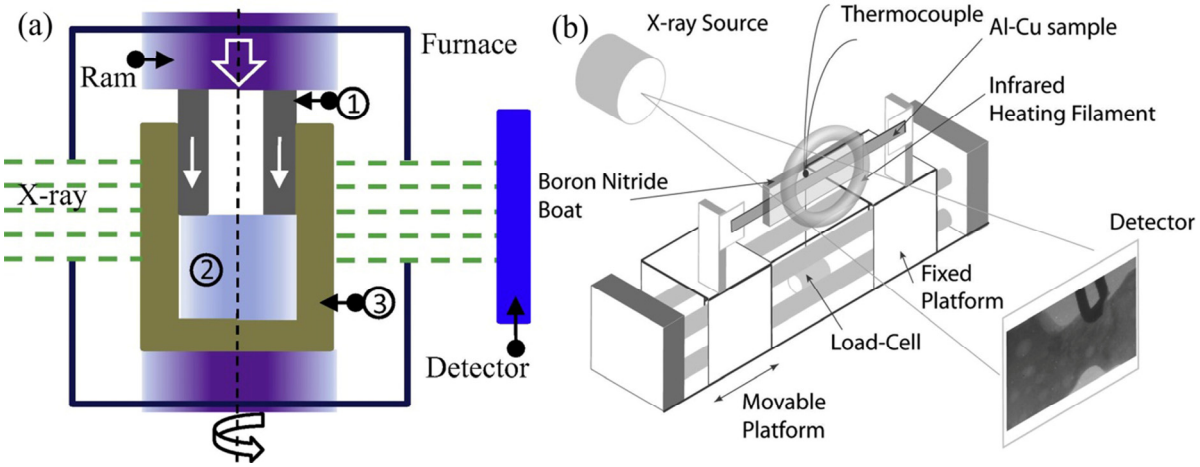

Fig. 19 Schematic of semi-solid deformation apparatus: (a) Compressive apparatus [107]; (b) Tensile apparatus [108] (1−Alumina tube; 2−Specimen; 3−Boron nitride holder)

the stress–strain response at 64%−93% solid fraction [116].

To understand the effect of heterogeneous nanoparticles (NPs) and microparticles (MPs) on the semisolid deformation behavior of Al−Cu alloys, WANG et al [118] quantified the semisolid deformation behavior of particle-free (P-free), NP-reinforced, and MP-reinforced Al−Cu composites. As shown in Fig. 20, for the P-free and NP-reinforced composites, the number and size of the voids decrease firstly and then increase with the increase of the true axial strain, while the number of voids in the MP-reinforced composites increases continuously during the deformation process. Furthermore, the number of pores in MP-reinforced composites (Figs. 20(h−k)) is much larger than that in P-free and NP-reinforced composites. They also found that, compared with the P-free and MP-reinforced Al−Cu composites, NP-reinforced composites exhibit the best hot-crack resistance due to the fine liquid channel, improved liquid channel distribution, refined dendrite grains, and low viscosity of the interdendrite liquid.

3.4.2 Semisolid tensile deformation behavior

In contrast to above semisolid compression, only few in situ studies were focused on the dynamic behavior during tensile processes via synchrotron X-ray imaging [108,119−122]. For example, using synchrotron tomography, TERZI et al [120] observed the microstructure evolution during a tensile process in a semisolid Al−8wt.%Cu alloy. It was found that the liquid fraction increases in the notched zone during the tensile process, and pores appear, gradually grow and finally form cracks. SISTANINIA et al [121] developed a hydromechanical granular model to describe the microstructure evolution during a tensile process in a semisolid Al–Cu alloy and reported a comparison

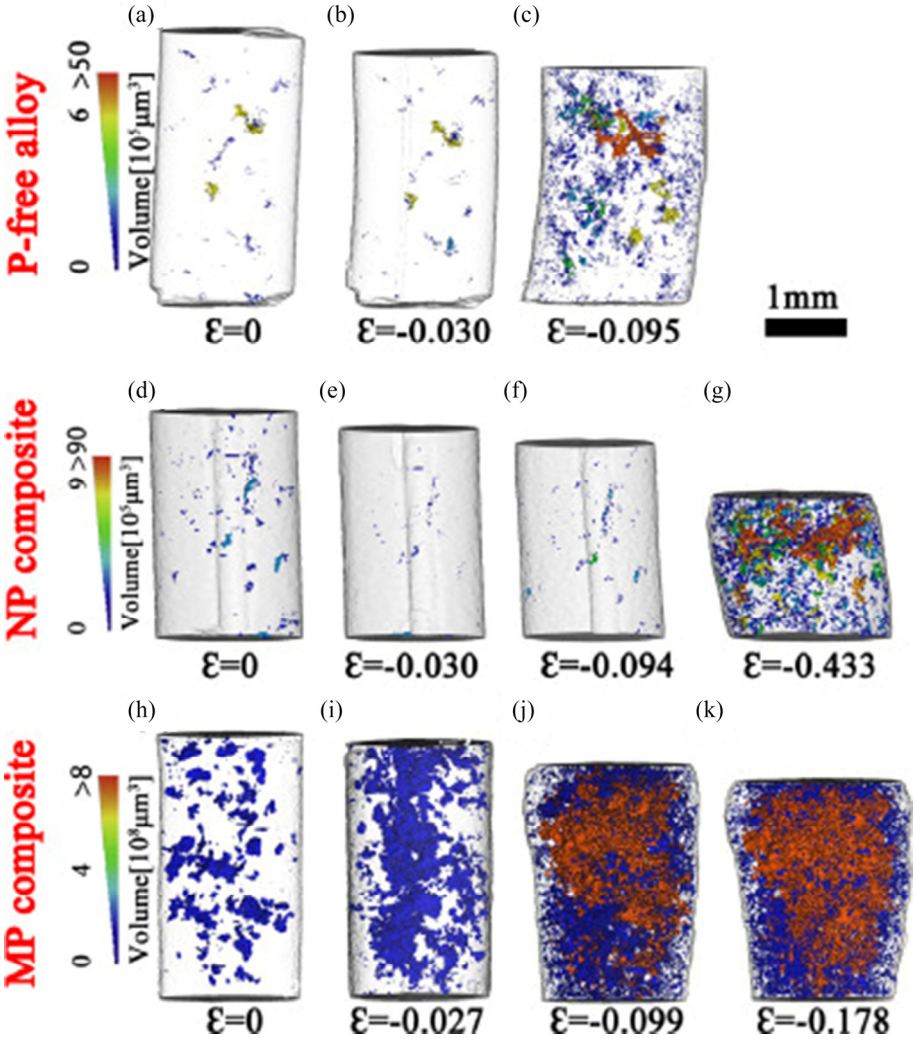

Fig. 20 Evolution of voids colored according to their sizes during semi-solid compression of three samples with increase in true axial strain [118]: (a−c) P-free alloy; (d−g) NP-reinforced composite; (h−k) MP-reinforced composite

of the results obtained via synchrotron tomography and the granular model prediction. If the deformed zone cannot be fed by the adjacent liquid, pores will form and grow during the deformation process. PHILLION et al [108] also directly observed the evolution of strain localization and pore coalescence during semisolid tensile deformation of an Al−12wt.%Cu alloy. They found that, when the solid fraction was low or moderate, interdendritic liquid feeding in the strain localization region occurred before crack formation, and they summarized three stage mechanisms of final failure during deformation. PUNCROBUTR et al [122] studied the damage evolution of a semisolid Al−Cu alloy under tensile conditions. As shown in Fig. 21(a), the internal pores firstly were formed, grew, and aggregated in the central region of the specimen, and then these pores grew toward the sample surface. The dynamic behaviors of these pores were closely related to the final failure (Fig. 21(b)).

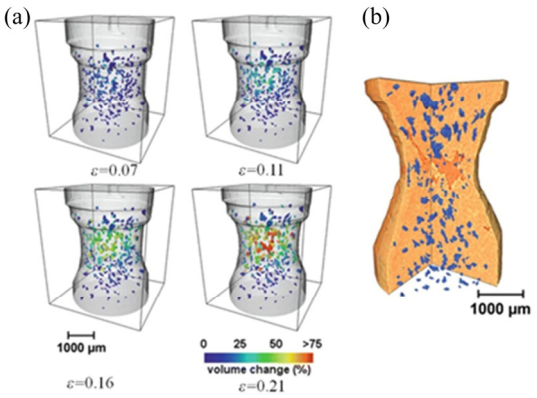

Fig. 21 3D rendering of internal damage where voids are colored by their percentage volume increase over initial size during early stage of hot tearing (a), and 3D rendering of solidification structure near final hot tearing (b) [122]

3.5 ADL apparatus

Figure 22 shows the sketch of an ADL device [123]. The sample is placed centrally on a nozzle, and it can be suspended stably by controlling the gas flow rate. The sample is heated and cooled by adjusting the laser frequency, and its temperature is measured using a pyrometer [124]. The aerodynamic method has many outstanding advantages [125,126]: (1) theoretically, all materials can be levitated; (2) the device is relatively simple and easy to operate; (3) there is no need for a feedback system to maintain balance; (4) it is convenient to control the sample temperature during melting and solidification. Therefore, the aerodynamic method has been used to fabricate metallic and nonmetallic materials, to investigate the thermophysical properties of superheated melt, and it is also an effective way to diminish heterogeneous nucleation.

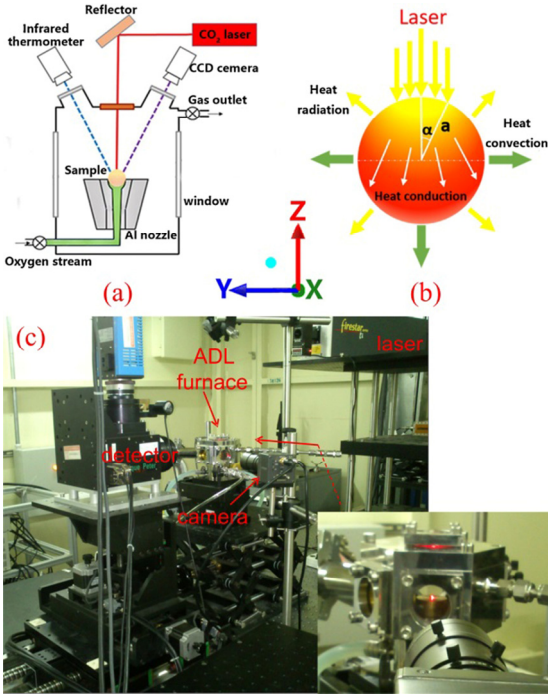

Fig. 22 Sketch of aerodynamic levitation set-up (a), illustration of heat transfer process between droplet and surrounding environment (b), and ADL device configuration at BL13W1 beam line of SSRF (c) [123]

3.5.1 Bubble and droplet behavior during heating

Using the ADL apparatus in combination with the high-brilliance synchrotron X-ray imaging technique, ZHANG et al [127] directly observed the bubble appearance and dissolution process in a superheated Al−Ca eutectic alloy melt. The Al−Ca sample is not completely suspended because the rotation of the levitated sample impairs the image quality. They found that the growth of a single isolated bubble followed a stochastic process, and the behavior of groups of bubbles was dominated by the Lifshitz–Slyozov–Wagner (LSW) diffusion.

Similarly, using the sessile drop method, LU et al [128] obtained the microstructure evolution during melting of an Al−Bi immiscible alloy. They placed an Al−Bi sample on a MgO sheet rather than a nozzle, while the other experimental procedures

were similar to those adopted in the above work regarding the aerodynamically levitated Al−Ca alloy. Bi solute coarsening and dissolution were investigated via synchrotron radiography. As shown in Fig. 23, the Bi-rich phase melts before the Al-rich phase with increasing temperature, and the Bi-rich phase is gradually released during the melting process of the surrounding Al phase. Eventually, all Bi phases dissolve in the Al matrix melt. Bi solute coarsening mainly stems from solute diffusion and the Stokes effect. Additionally, the solute concentration around Bi droplets of different sizes is different.

3.5.2 Interaction of bubbles with segregation in solidifying Al−Bi alloys

LU et al [129] controlled the bubble evolution and segregation morphology in the Al-based immiscible alloys. After the Al−Bi alloy was superheated through a CO_2 laser, the behavior of hydrogen bubbles and minor droplets during solidification was investigated via synchrotron radiography under a cooling rate of 0.7 K/s. It was shown that the segregated Bi atoms can change the bubble behavior, resulting in the size distribution of the bubbles following neither the Gaussian nor the LSW distribution. The growth behavior of groups of Bi droplets is in good agreement with the logistic model. They also presented a full view of the microstructure evolution during solidification of an Al−10wt.%Bi immiscible alloy under higher cooling rate [130]. They found that a proportion of the Bi solute segregated onto the alloy surface before the occurrence of the liquid phase separation, and the Bi atoms settled down in the alloy melt due to melt convection. Subsequently, the Marangoni effect played a leading role in droplet coagulation in the early stage of the liquid decomposition, while the Stokes effect dominated in the later stage, when the droplets grew to a critical value. Furthermore, the size distribution of the Bi-rich droplets was found to follow the Gaussian distribution under higher cooling rate [130].

Clearly, the applied casting condition determines the final solidification microstructure. Furthermore, the number of bubbles grows with increasing the cooling rate, while their size decreases [131]. It has been proven that bubbles have a significant impact on solute segregation and the subsequent liquid phase separation [131−133]. Bubble-induced solute segregation occurs in many Al alloys during solidification [132]. Here, the amount of segregated Bi solute determines whether the liquid phase separation process occurs or not (Fig. 24). As shown in Fig. 24, if the amount of segregated Bi on the bubble surface is sufficiently large to shift the matrix melt concentration to Zone I in the Al−Bi alloy phase diagram, the liquid phase separation phenomenon does not happen during

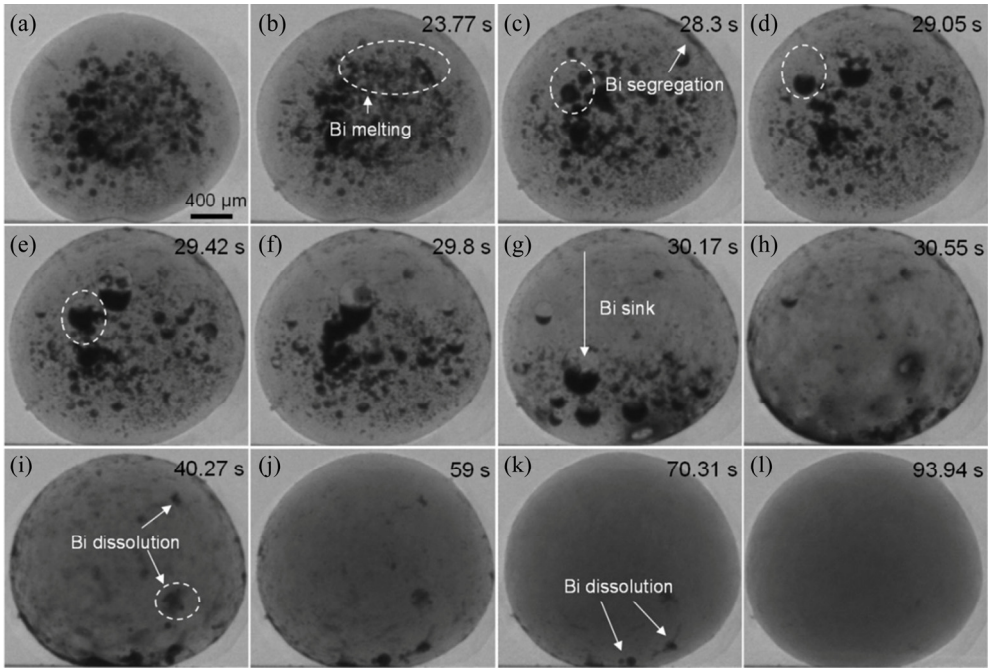

Fig. 23 Original structure of Al−10wt.%Bi alloy particle before melting (a) and microstructural evolution in melting Al−10wt.%Bi immiscible alloy (b−l) [128]

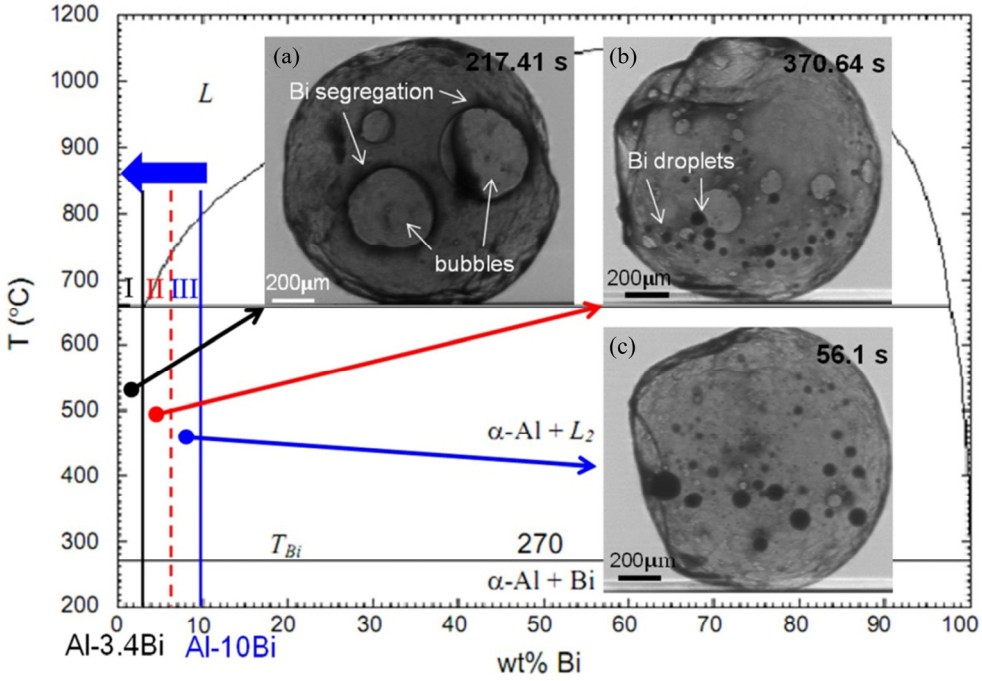

Fig. 24 Sketch of effect of bubbles on liquid phase separation based on Al−Bi alloy phase diagram [134]: (a) Adapted from Ref. [131]; (b) Adapted from Ref. [129]; (c) Adapted from Ref. [133]

solidification. Additionally, if the amount of segregated Bi is very small, the matrix melt concentration is located in Zone III in Fig. 24; large amounts of Bi droplets and large-sized Bi droplets appear during the liquid phase separation process [133].

3.6 LAM apparatus

Figure 25 shows the sketch of a typical LAM setup for synchrotron radiography [135]. As shown in Fig. 25, the setup mainly consists of four parts: a chamber, a laser system, a laser enclosure, and an infrared (IR) reflector. LAM is one of most advanced material manufacturing technologies. With the help of a laser, LAM causes powder materials to melt and solidify layer by layer rapidly, and the fully compact integral components are formed directly from 3D digital models [136,137]. With the rapid development of laser and computer technology, a series of different LAM technologies and equipment gradually emerged, such as selective maser melting [138], direct metal deposition technology [139], and shape deposition manufacturing [140]. Compared with the traditional manufacturing methods, such as casting, forging, and welding, LAM technologies have the following advantages [141]: (1) they can realize integrated forming of high-performance alloys, and the manufacturing process is very short; (2) the rapid solidification structure can be easily formed with uniform and fine grains, and the prepared metal components have excellent properties; (3) near net forming, and there is almost no need of the subsequent machining; (4) the laser can melt a variety of refractory metals. At present, the LAM technology is recognized as a key technology for obtaining major high-end equipment in nuclear power plants, shipbuilding, aviation and aerospace industry, as well as other fields [141]. Although great progress has been made on LAM in recent years, the defect formation, the interaction between lasers and powder materials, the evolution dynamics of molten pool, and the solidification microstructure evolution are still unclear.

3.6.1 Pore formation mechanism

To uncover the keyhole pore formation mechanism during the laser powder bed fusion (LPBF) process, ZHAO et al [142−144] made a deep study of the LPBF process in Ti−6Al−4V alloy using high-speed X-ray imaging technique. They found that, although the keyhole pores had a tendency to float up at the bottom of melt pool, they were still confined by the solidification front, and finally became defects. Further research showed

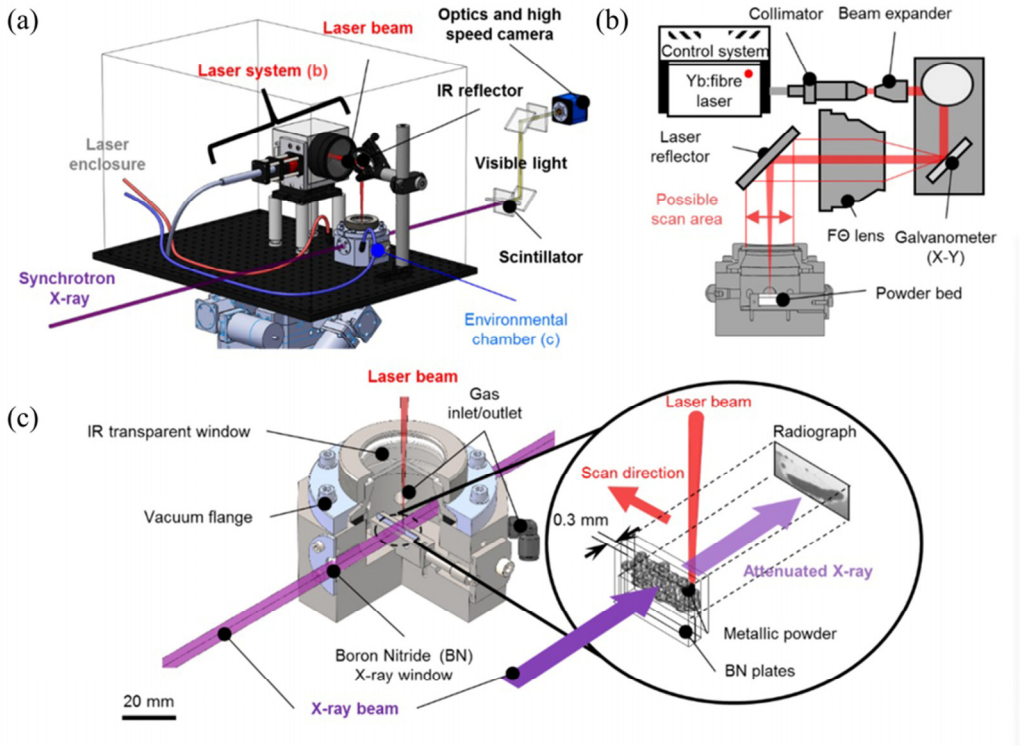

Fig. 25 Experimental setup for in-situ laser additive manufacturing process replicator (LAMPR) [135]

that keyhole pores were related to acoustic waves in the molten pool. The critical instability at the root of a keyhole releases acoustic waves that rapidly drive pores away from the keyhole. HOJJATZADEH et al [145] and MARTIN et al [146,147] also direct observed the pores formation and revealed many new formation mechanisms of pores during LAM.

3.6.2 Molten pool evolution

To reveal the dynamics of molten pool evolution, LEUNG et al [135,148,149] used synchrotron X-ray imaging to monitor the molten pool morphology during LAM. Combining the LAM apparatus and synchrotron radiography, they directly observed the pore formation, dissolution, migration, bursting, and molten pool coalescence behavior during LAM of an Invar 36 (Fig. 26). They found that the Marangoni convection can increase the molten pool oscillations and developed a model map that could predict the evolution of the melt characteristics and melt trace morphology. Furthermore, by comparing unoxidized and oxidized Invar 36 powder during LAM, they studied the effect of powder oxidation on defect formation. The oxygen content of the oxidized powder was found to be sufficiently high to alter the sign of the temperature dependence of the surface tension, which resulted in a change in the direction of Marangoni convection in melt pool. The formation of power spatter and droplet spatter mainly depended on the laser beam position [145]. Both indirect laser-induced gas expansion and laser-induced vapor can lead to droplet spatter during LAM. Besides, GUO et al [150,151] also focused on the melt flow dynamics during the LAM process.

Very recently, combining synchrotron radiation X-ray imaging and diffraction, CHEN et al [152] investigated the melt-pool dynamics and solidification structure evolution during directed energy deposition additive manufacturing (DED-AM) of an IN718 superalloy. They revealed the phase transformation sequence and quantified the heat transfer kinetics. They also confirmed that the Marangoni convection dominates the melt-pool flow. And they further revealed the effects of the processing parameters (powder feed rate, laser power, and traverse speed) on the melt-pool evolution and microstructure formation during DED-AM of SS316L and Ti-6242 alloy [153−155]. It was shown that the laser power dominates the build efficiency, and the pore pushing phenomena mainly originated from fluid flow.

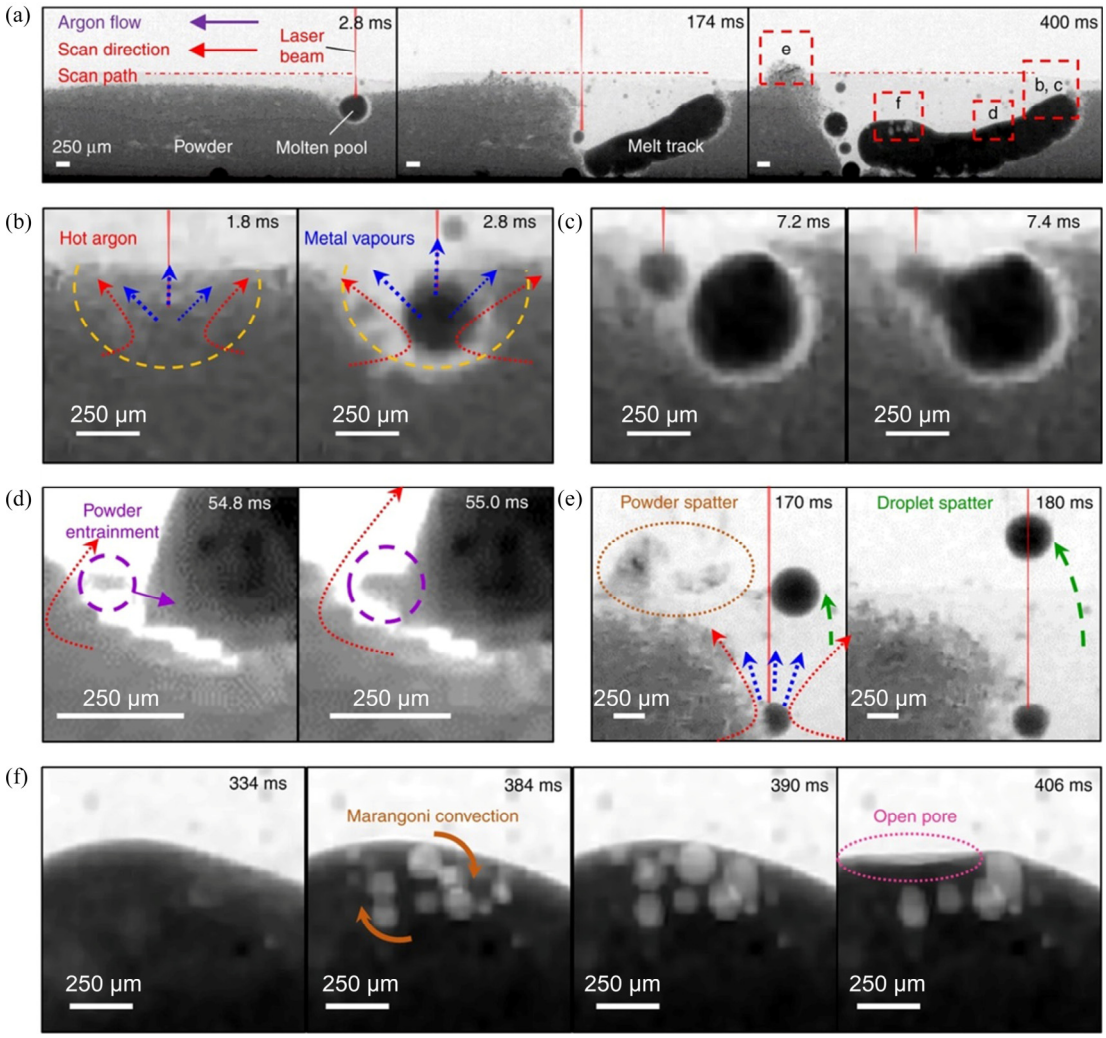

Fig. 26 Time-series radiographs acquired during LAM of Invar 36 single-layer melt track (MT1) under P=209 W, v=13 mm/s and LED=16.1 J/mm [135]

4 Summary and outlook

The synchrotron radiation X-ray imaging technique has been widely employed in metal solidification research owing to its numerous advantages, such as high spatial and temporal resolutions, high penetrability, nondestructive capabilities, and the possibility to obtain dynamic visualization. Combined with the advanced solidification apparatuses, real-time images make it possible to visualize the microstructure evolution, defect formation, crack initiation, and propagation in the metals. They also provide valuable information to establish the relationship between external fields and the solidification behavior, which can enrich the solidification theory. Further development of the solidification apparatuses and synchrotron radiation X-ray imaging should involve the following aspects:

(1) Combining multiphysical apparatuses and synchrotron radiation X-ray imaging to understand the solidification behavior of metals under two or more external fields. Coupling of physical fields, i.e., thermal, mechanical, electrical, magnetic, ultrasonic, and oxygen partial pressure, may significantly change the solidification microstructure of metals and result in superior properties. Therefore, it is interesting to apply imaging techniques to understand the solidification process of metals under multiple fields. Such research will depend on the development of apparatuses with the possibility to simultaneously apply more than one field.

(2) Improving the resolution of the synchrotron radiation nano-CT, 3D, or 4D imaging to reveal the solidification microstructure evolution at nanoscale. This may facilitate understanding of

the nucleation stage during solidification.

(3) Although not covered in this review, combining X-ray radiography and other characterization techniques, such as fluorescence, wide angle X-ray scattering, Laue diffraction, and diffraction imaging, can be very promising in studying the solidification process. Related studies are available for readers who are interested in the above combined techniques.

(4) Developing an ultrafast X-ray imaging technique and fast image processing to obtain dynamic details of the solidification process. This will generate an incredibly large number of images; therefore, machine learning will be required to enable fast image processing.

(5) Laboratory X-ray radiography devices at space station will be very important supplement for revealing principles of metal solidification under microgravity.

Acknowledgments

This work is supported by the National Natural Science Foundation of China for Excellent Young Scholars (No. 51922068), the National Natural Science Foundation of China (Nos. 51821001, 51904186), and the fund of the State Key Laboratory of Solidification Processing in NWPU, China (No. SKLSP202102). The support of synchrotron radiation phase-contrast imaging by the BL13W1 beam line of Shanghai Synchrotron Radiation Facility (SSRF), China, is gratefully acknowledged.

References

[1] GUO Qiang, LI Zhi-qiang, ZHAO Lei, LI Zan, FENG Si-wen, ZHANG Di. Metal matrix composites with microstructural architectures [J]. Materials China, 2016, 35: 641−650. (in Chinese)

[2] CAO Fei, WANG Tong-min. Applications of synchrotron radiation imaging technology in metallic materials research [J]. Materials China, 2017, 36: 161−167. (in Chinese)

[3] GLICKSMAN M E. Principles of solidification: An introduction to modern casting and crystal growth concepts [M]. Springer Science & Business Media, 2010.

[4] SHUAI San-san, WANG Jiang, REN Zhong-ming. Application of synchrotron X-ray imaging in solidification of metallic materials [J]. Materials China, 2019, 38: 68−76. (in Chinese)

[5] WANG Yong-biao, JIA Sen-sen, WEI Ming-guang, PENG Li-ming, WU Yu-juan, LIU Xin-tian. Research progress on solidification structure of alloys by synchrotron X-ray radiography: A review [J]. Journal of Magnesium and Alloys, 2020, 8: 396−413.

[6] DING Zong-ye, ZHANG Nai-fang, YU Liao, LU Wen-quan, LI Jian-guo, HU Q D. Recent progress in metallurgical bonding mechanisms at the liquid/solid interface of dissimilar metals investigated via in situ X-ray imaging technologies [J]. Acta Metallurgica Sinica (English Letters), 2021, 34: 145−168.

[7] ZHU Jing, WANG Tong-min, CAO Fei, FU Hong-wang, FU Ya-nan, XIE Hong-lan, XIAO Ti-qiao. Real-time observation on evolution of droplets morphology affected by electric current pulse in Al−Bi immiscible alloy [J]. Journal of Materials Engineering and Performance, 2013, 22: 1319−1323.

[8] WANG W L, LI Z Q, WEI B. Macrosegregation pattern and microstructure feature of ternary Fe−Sn−Si immiscible alloy solidified under free fall condition [J]. Acta Materialia, 2011, 59: 5482−5493.

[9] SHI R P, WANG Y, WANG C P, LIU X J. Self-organization of core-shell and core-shell-corona structures in small liquid droplets [J]. Applied Physics Letters, 2011, 98: 204106.

[10] SHI R P, WANG C P, WHEELER D, LIU X J, WANG Y. Formation mechanisms of self-organized core/shell and core/shell/corona microstructures in liquid droplets of immiscible alloys [J]. Acta Materialia, 2013, 61: 1229−1243.

[11] ZhANG Li, WANG Nan, ZHENG Ya-ping, YAO Wen-jing. Phase separation in PVME-H_2O transparent system [J]. Procedia Engineering, 2012, 27: 1508−1517.

[12] ZHAI Wei, WANG Nan, Wei Bing-Bo. Direct observation of phase separation in binary monotectic solution [J]. Acta Physica Sinica, 2007, 56(4): 2353−2358. (in Chinese)

[13] WANG N, ZHANG L, ZHENG Y P, YAO W J. Shell phase selection and layer numbers of core-shell structure in monotectic alloys with stable miscibility gap [J]. Journal of Alloys and Compounds, 2012, 538: 224−229.

[14] PENG Yin-li, HAN San-xuan, TIAN Li-li, WANG Nan. In situ investigation of minor-phase globule collision and the structure in a droplet-shaped immiscible alloy [J]. Materials Letters, 2019, 254: 222−225.

[15] MELENDEZ A J, BECKERMANN C. Measurements of dendrite tip growth and sidebranching in succinonitrile-acetone alloys [J]. Journal of Crystal Growth, 2012, 340: 175−189.

[16] SCHAFFER P L, MATHIESEN R H, ARNBERG L. L_2 droplet interaction with α-Al during solidification of hypermonotectic Al−8wt.%Bi alloys [J]. Acta Materialia, 2009, 57: 2887−2895.

[17] SCHAFFER P L, MATHIESEN R H, ARNBERG L, DI SABATINO M D, SNIGIREV A. In-situ investigation of spinodal decomposition in hypermonotectic Al−Bi and Al−Bi−Zn alloys [J]. New Journal of Physics, 2008, 10: 1−16.

[18] MAI Zhen-hong. Synchrotron radiation light source and application [M]. Beijing: Science Press, 2013. (in Chinese)

[19] XIAO Ti-qiao, XIE Hong-lan, DENG Biao, DU Guo-hao, CHEN Rong-chang. Progresses of X-ray imaging methodology and its applications at Shanghai synchrotron radiation facility [J]. Acta Optica Sinica, 2014, 34(1): 0100001. (in Chinese)

[20] REINHART G, MANGELINCK-NOËL N, NGUYEN-THI H, SCHENK T, GASTALDI J, BILLIA B, PINO P, HÄRTWIG J, BARUCHEL J. Investigation of columnar-

equiaxed transition and equiaxed growth of aluminium based alloys by X-ray radiography [J]. Materials Science and Engineering A, 2005, 413/414: 384−388.

[21] THI H N, REINHART G, BUFFET A, SCHENK T, MANGELINCK-NOËL N, JUNG H, BERGEON N, BILLIA B, HÄRTWIG J, BARUCHEL J. In situ and real-time analysis of TGZM phenomena by synchrotron X-ray radiography [J]. Journal of Crystal Growth, 2008, 310: 2906−2914.

[22] MATHIESEN R H, ARNBERG L, BLEUET P, SOMOGYI A. Crystal fragmentation and columnar-to-equiaxed transitions in Al−Cu studied by synchrotron X-ray video microscopy [J]. Metallurgical and Materials Transactions A, 2006, 37: 2515−2524.

[23] BOGNO A, NGUYEN-THI H, BUFFET A, REINHART G, BILLIA B, MANGELINCK-NOËL N, BERGEON N, BARUCHEL J, SCHENK T. Analysis by synchrotron X-ray radiography of convection effects on the dynamic evolution of the solid-liquid interface and on solute distribution during the initial transient of solidification [J]. Acta Materialia, 2011, 59: 4356−4365.

[24] ARFELLI F, BONVICINI V, BRAVIN A, CANTATORE G, CASTELLI E, PALMA L D, MICHIEL M D, FABRIZIOLI M, LONGO R, MENK R H, OLIVO A, PANI S, PONTONI D, POROPAT P, PREST M, RASHEVSKY A, RATTI M, RIGON L, TROMBA G, VACCHI A, VALLAZZA E, ZANCONATI F. Mammography with synchrotron radiation: Phase-detection techniques [J]. Radiology, 2000, 215: 286−293.

[25] MOMOSE A. Demonstration of phase-contrast X-ray computed-tomography using an X-ray interferometer [J]. Nuclear Instruments and Methods in Physics Research Section A, 1995, 352: 622−628.

[26] DAVIS T J, GAO D, GUREYEV T E. Phase-contrast imaging of weakly absorbing materials using hard X-rays [J]. Nature, 1995, 373: 595−598.

[27] WEITKAMP T, DIAZ A, NOHAMMER B, PFEIFFER F, ROHBECK T, CLOETENS P, STAMPANONI M, DAVID C. Hard X-ray phase imaging and tomography with a grating interferometer [C]//Proceeding of SPIE. Denver, Colorado, USA, 2004, 5535: 137−142.

[28] WILKINS S W, GUREYEV T E, GAO D, POGANY A, STEVENSON A W. Phase-contrast imaging using polychromatic hard X-rays [J]. Nature, 1996, 384: 335−338.

[29] SUN Si-yu, HU Qiao-dan, LU Wen-quan, DING Zong-ye, XIA Ming-xu, LI Jian-guo. In situ observation on bubble behavior of solidifying Al−Ni alloy under the interference of intermetallic compounds [J]. Metallurgical and Materials Transactions A, 2018, 49: 4429−4434.

[30] LI B, BRODY H D, KAZIMIROV A. Real-time observation of dendrite coarsening in Sn−13%Bi alloy by synchrotron microradiography [J]. Physical Review E, 2004, 70: 062602.

[31] LI B, BRODY H D, KAZIMIROV A. Real time synchrotron microradiography of dendrite coarsening in Sn−13wt.%Bi alloy [J]. Metallurgical and Materials Transactions A, 2007, 38: 599−605.

[32] RUVALCABA D, MATHIESEN R H, ESKIN D G, ARNBERG L, KATGERMAN L. In-situ analysis of coarsening during directional solidification experiments in high-solute aluminum alloys [J]. Metallurgical and Materials Transactions B, 2009, 40: 312−316.

[33] YASUDA H, OHNAKA I, KAWASAKI K, SUGIYAMA A, OHMICHI T, IWANE J, UMETANI K. Direct observation of stray crystal formation in unidirectional solidification of Sn−Bi alloy by X-ray imaging [J]. Journal of Crystal Growth, 2004, 262: 645−652.

[34] YASUDA H, YAMAMOTO Y, NAKATSUKA N, YOSHIYA M, NAGIRA T, SUGIYAMA A, OHNAKA I, UESUGI K, UMETANI K. In situ observation of solidification phenomena in Al−Cu and Fe−Si−Al alloys [J]. International Journal of Cast Metals Research, 2009, 22: 15−21.

[35] RUVALCABA D, MATHIESEN R H, ESKIN D G, ARNBERG L, KATGERMAN L. In situ observations of dendritic fragmentation due to local solute-enrichment during directional solidification of an aluminum alloy [J]. Acta Materialia, 2007, 55: 4287−4292.

[36] ARNBERG L, MATHIESEN R H. The real-time, high-resolution X-ray video microscopy of solidification in aluminum alloys [J]. JOM, 2007, 59: 20−26.

[37] NGUYEN-THI H, BOGNO A, REINHART G, BILLIA B, MATHIESEN R H, ZIMMERMANN G, HOULTZ Y, LÖTH K, VOSS D, VERGA A, de PASCALE F D. Investigation of gravity effects on solidification of binary alloys with in situ X-ray radiography on earth and in microgravity environment [J]. Journal of Physics: Conference Series, 2011, 327: 012012.

[38] GIBBS J W, TOURRET D, GIBBS P J, IMHOFF S D, GIBBS M J, WALKER B A, FEZZAA K, CLARKE A J. In Situ X-Ray Observations of dendritic fragmentation during directional solidification of a Sn−Bi alloy [J]. Jom, 2016, 68: 170−177.

[39] SCHENK T, THI H N, GASTALDI J, REINHART G, CRISTIGLIO V, MANGELINCK-NOËL N N, KLEIN H, HÄRTWIG J, GRUSHKO B, BILLIA B, BARUCHEL J. Application of synchrotron X-ray imaging to the study of directional solidification of aluminium-based alloys [J]. Journal of Crystal Growth, 2005, 275: 201−208.

[40] NGUYEN-THI H, REINHART G, MANGELINCK-NOËL N, JUNG H, BILLIA B, SCHENK T, GASTALDI J, HÄRTWIG J, BARUCHEL J. In-situ and real-time investigation of columnar-to-equiaxed transition in metallic alloy [J]. Metallurgical and Materials Transactions A, 2007, 38: 1458−1464.

[41] DONG Qing, ZHANG Jiao, DONG Jin-fang, XIE Hong-lan, LIU Zhi-jun, DAI Yong-bing, LIU Yang, SUN Bao-de. In situ observation of columnar-to-equiaxed transition in directional solidification using synchrotron X-radiation imaging technique [J]. Materials Science and Engineering A, 2011, 530: 271−276.

[42] LI Fa-guo, DONG Qing, ZHANG Jiao, DAI Yong-bing, FU Ya-nan, XIE Hong-lan, YIN Fu-cheng, SUN Bao-de. In situ study on columnar-equiaxed transition and anaxial columnar dendrite growth of Al−15%Cu alloy by synchrotron radiography [J]. Transactions of Nonferrous Metals Society of China, 2014, 24: 2112−2116.

[43] KANG Mao-dong, GAO Hai-yan, SHU Da, WANG Jun, LI Fa-guo, FU Ya-nan, LING Li-shi-bao, SUN Bao-de. In situ and real-time observation of the solidification process of Al−20mass.%Cu Alloy by Synchrotron X-ray Radiography [J]. Materials Transactions, 2014, 55: 774−778.

[44] LI B, BRODY H D, KAZIMIROV A. Synchrotron microradiography of temperature gradient zone melting in directional solidification [J]. Metallurgical and Materials Transactions A, 2006, 37: 1039−1044.

[45] BOGNO A, REINHART G, BUFFET A, THI H N, BILLIA B, SCHENK T, MANGELINCK-NOËL N, BERGEON N, BARUCHEL J. In situ analysis of the influence of convection during the initial transient of planar solidification [J]. Journal of Crystal Growth, 2011, 318: 1134−1138.

[46] YASUDA H, NAGIRA T, YOSHIYA M, NAKATSUKA N, SUGIYAMA A, UESUGI K, UMETANI K. Development of X-ray imaging for observing solidification of carbon steels [J]. ISIJ International, 2011, 51: 402−408.

[47] REINHART G, GRANGE D, ABOU-KHALIL L, MANGELINCK-NOËL N, NIANE N T, MAGUIN V, GUILLEMOT G, GANDIN C A, NGUYEN-THI H. Impact of solute flow during directional solidification of a Ni-based alloy: In-situ and real-time X-radiography [J]. Acta Materialia, 2020, 194: 68−79.

[48] DONG Yuan-hao, SHUAI San-san, ZHENG Tian-xiang, CAO Jia-wei, CHEN Chao-yue, WANG Jiang, REN Zhong-ming. In-situ observation of solid-liquid interface transition during directional solidification of Al−Zn alloy via X-ray imaging [J]. Journal of Materials Science & Technology, 2020, 39: 113−123.

[49] LIOTTI E, ARTETA C, ZISSERMAN A, LUI A, LEMPITSKY V, GRANT P S. Crystal nucleation in metallic alloys using x-ray radiography and machine learning [J]. Science advances, 2018, 4: eaar4004.

[50] JIA Yi-wang, HUANG Hai-jun, FU Ya-nan, ZHU Guo-liang, SHU Da, SUN Bao-de, STJOHN D H. An in situ investigation of the solute suppressed nucleation zone in an Al−15wt.%Cu alloy inoculated by Al−Ti−B [J]. Scripta Materialia, 2019, 167: 6−10.

[51] JIA Yi-wang, WANG Dong-hong, FU Ya-nan, DONG An-ping, ZHU Guo-liang, SHU Da, SUN Bao-de. In situ investigation of the heterogeneous nucleation sequence in Al-15 weight percent Cu alloy inoculated by Al−Ti−B [J]. Metallurgical and Materials Transactions A, 2019, 50: 1795−1804.

[52] JIA Yi-wang, WANG Shu-bin, HUANG Hai-jun, WANG Dong-hong, FU Ya-nan, ZHU Guo-liang, DONG An-ping, Du D F, SHU Da, SUN Bao-de. In situ observation of the Zr poisoning effect in Al alloys inoculated by Al−Ti−B [J]. Metallurgical and Materials Transactions A, 2018, 49: 4771−4784.

[53] XU Jin, LI Yang, MA Ke, FU Ya-nan, GUO Enyu, CHEN Zong-ning, GU Qin-fen, HAN Yue-xing, WANG Tong-min, LI Qian. In-situ observation of grain refinement dynamics of hypoeutectic Al−Si alloy inoculated by Al−Ti−Nb−B alloy [J]. Scripta Materialia, 2020, 187: 142−147.

[54] BOGNO A, NGUYEN-THI H, REINHART G, BILLIA B, BARUCHEL J. Growth and interaction of dendritic equiaxed grains: In situ characterization by synchrotron X-ray radiography [J]. Acta Materialia, 2013, 61: 1303−1315.

[55] YASUDA H, NAGIRA T, YOSHIVA M, SUGIYAMA A, NAKATSUKA N, KIIRE M, UESUGI M, UESUGI K, UMETANI K, KAJIWARA K. Massive transformation from δ phase to γ phase in Fe−C alloys and strain induced in solidifying shell [J]. IOP Conference Series: Materials Science and Engineering, 2012, 33: 012036.

[56] GIBBS J W, MOHAN K A, GULSOY E B, SHAHANI A J, XIAO X, BOUMAN C A, DE GRAEF M, VOORHEES P W. The three-dimensional morphology of growing dendrites [J]. Scientific Reports, 2015, 5: 11824.

[57] AZEEM M A, LEE P D, PHILLION A B, KARAGADDE S, ROCKETT P, ATWOOD R C, COURTOIS L, RAHMAN K M, DYE D. Revealing dendritic pattern formation in Ni, Fe and Co alloys using synchrotron tomography [J]. Acta Materialia, 2017, 128: 241−248.

[58] YU J M, WANDERKA N, RACK A, DAUDIN R, BOLLER E, MARKÖTTER H, MANZONI A, VOGEL F, ARLT T, MANKE I, BANHART J. Formation of intermetallic δ phase in Al−10Si−0.3Fe alloy investigated by in situ 4D X-ray synchrotron tomography [J]. Acta Materialia, 2017, 129: 194−202.

[59] FENG S K, LIOTTI E, LUI A, WILSON M D, CONNOLLEY T, MATHIESEN R H, GRANT P S. In-situ X-ray radiography of primary Fe-rich intermetallic compound formation [J]. Acta Materialia, 2020, 196: 759−769.

[60] LI Zheng-yang, ZHU Ming-fang, DAI Ting. Modeling of microporosity formation in an Al−7%Si alloy [J]. Acta Metallurgica Sinica, 2013, 49: 1032−1040.

[61] LU Wen-quan, ZHANG Nai-fang, DING Zong-ye, YANG Fan, HU Qiao-dan, ZENG Long, LI Jian-guo. Bubble growth, intermetallic compounds dissolution and their interactions during heating of an Al−5wt.%Mn alloy by in-situ synchrotron radiography [J]. Journal of Alloys and Compounds, 2020, 822: 153554.

[62] LU Wen-quan, ZHANG Nai-fang, REN Neng, DING Zong-ye, YANG Fan, HU Qiao-dan, LI Jian-guo. Bubble-induced formation of new intermetallic compounds in an Al−Mn alloy during heating observed by synchrotron radiography [J]. Materialia, 2021, 15: 100991.

[63] LI Hai-long, AN Rong, WANG Chun-qing, JIANG Zhi. In situ quantitative study of microstructural evolution at the interface of $Sn_{3.0}Ag_{0.5}Cu$/Cu solder joint during solid state aging [J]. Journal of Alloys and Compounds, 2015, 634: 94−98.

[64] MOHD SALLEH M A A, MCDONALD S D, YASUDA H, SUGIYAMA A, NOGITA K. Rapid Cu_6Sn_5 growth at liquid Sn/solid Cu interfaces [J]. Scripta Materialia, 2015, 100: 17−20.

[65] HUANG M L, YANG F, ZHAO N, ZHANG Z J. In situ study on dissolution and growth mechanism of interfacial Cu_6Sn_5 in wetting reaction [J]. Materials Letters, 2015, 139: 42−45.

[66] DING Zong-ye, HU Qiao-dan, LU Wen-quan, SUN Si-yu, XIA Ming-xu, LI Jian-guo. In-situ observation on the diversified morphology and growth behavior of Al_3Ni phase at the liquid Al/solid Ni interface [J]. Metallurgical and Materials Transactions A, 2018, 49: 1486−1491.

[67] DING Zong-ye, HU Qiao-dan, LU Wen-quan, SUN Si-yu, XIA Ming-xu, LI Jian-guo. In situ observation on the formation of intermetallics compounds at the interface of liquid Al/solid Ni [J]. Scripta Materialia, 2017, 130: 214−218.

[68] DING Zong-ye, HU Qiao-dan, LU Wen-quan, GE Xuan, CAO Sheng, SUN Si-yu, YANG Tian-xing, XIA Ming-xu, LI

Jian-guo. Microstructural evolution and growth behavior of intermetallic compounds at the liquid Al/solid Fe interface by synchrotron X-ray radiography [J]. Materials Characterization, 2018, 136: 157−164.

[69] WANG Tong-min, CAO Fei, ZHOU Peng, KANG Hui-jun, CHEN Zong-ning, FU Ya-nan, XIAO Ti-qiao, HUANG Wan-xia, YUAN Qing-xi. Study on diffusion behavior and microstructural evolution of Al/Cu bimetal interface by synchrotron X-ray radiography [J]. Journal of Alloys and Compounds, 2014, 616: 550−555.

[70] DING Zong-ye, HU Qiao-dan, CAO Sheng, YANG Tian-xi, YANG Fan, YU Liao, LU Wen-quan, ZHANG Nai-fang, LI Jian-guo. In situ analysis of multiphase compounds at the liquid Al-solid Cu interface: formation sequence, growth kinetics and critical thickness [J]. Metallurgical and Materials Transactions A, 2020, 51: 5245−5256.

[71] QU Lin, ZHAO Ning, MA Hai-tao, ZHAO Hui-jing, HUANG Ming-liang. In situ study on the effect of thermomigration on intermetallic compounds growth in liquid-solid interfacial reaction [J]. Journal of Applied Physics, 2014, 115: 204907.

[72] MERTENS J C E, KIRUBANANDHAM A, CHAWLA N. Electromigration mechanisms in Sn-0.7Cu/Cu couples by four dimensional (4D) X-ray microtomography and electron backscatter diffraction (EBSD) [J]. Acta Materialia, 2016, 102: 220−230.

[73] DING Zong-ye, HU Qiao-dan, LU Wen-quan, ZHANG Nai-fang, GE Xuan, CAO Sheng, YANG Tian-xing, XIA Ming-xu, LI Jian-guo. Continuous morphological transition and its mechanism of Al_3Ni phase at the liquid–solid interface during solidification [J]. Metallurgical and Materials Transactions A, 2019, 50: 556−561.

[74] YU Liao, HU Qiao-dan, DING Zong-ye, YANG Fan, LU Wen-quan, ZHANG Nai-fang, CAO Sheng, LI Jian-guo. Effect of cooling rate on the 3D morphology of the proeutectic Al_3Ni intermetallic compound formed at the Al/Ni interface after solidification [J]. Journal of Materials Science & Technology, 2021, 69: 60−68.

[75] XIAN J W, BELYAKOV S A, OLLIVIER M, NOGITA K, YASUDA H, GOURLAY C M. Cu_6Sn_5 crystal growth mechanisms during solidification of electronic interconnections [J]. Acta Materialia, 2017, 126: 540−551.

[76] MOHD SALLEH M A A, GOURLAY C M, XIAN J W, BELYAKOV S A, YASUDA H, MCDONALD S D, NOGITA K. In situ imaging of microstructure formation in electronic interconnections [J]. Scientific reports, 2017, 7: 40010.

[77] MA H R, KUNWAR A, SHANG S Y, JIANG C R, WANG Y P, MA H T, ZHAO N. Evolution behavior and growth kinetics of intermetallic compounds at Sn/Cu interface during multiple reflows [J]. Intermetallics, 2018, 96: 1−12.

[78] ZHANG Nai-fang, HU Qiao-dan, YANG Fan, LU Wen-quan, DING Zong-ye, CAO Sheng, YU Liao, GE Xuan, LI Jian-guo. Effect of Si on the growth behavior of the Fe_2Al_5 phase at Al−xSi (liquid)/Fe (solid) interface during holding by in situ synchrotron radiography [J]. Metallurgical and Materials Transactions A, 2020, 51: 2711−2718.

[79] WANG Tong-min, XU Jing-jing, XIAO Ti-qiao, XIE Hong-lan, LI Jun, LI Ting-ju, CAO Zhi-qiang. Evolution of dendrite morphology of a binary alloy under an applied electric current: An in situ observation [J]. Physical Review E, 2010, 81: 042601.

[80] ZHU Jing, WANG Tong-min, CAO Fei, HUANG Wan-xia, FU Hong-wang, CHEN Zong-ning. Real time observation of equiaxed growth of Sn−Pb alloy under an applied direct current by synchrotron microradiography [J]. Materials Letters, 2012, 89: 137−139.

[81] WANG Tong-min, ZHU Jing, KANG Hui-jun, CHEN Zong-ning, FU Ya-nan, HUANG Wan-xia, XIAO Ti-qiao. In situ synchrotron X-ray imaging on morphological evolution of dendrites in Sn−Bi hypoeutectic alloy under electric currents [J]. Applied Physics A, 2014, 117: 1059−1066.

[82] ZHU Jing, WANG Tong-min, XU Jing-jing, CHEN Zong-ning, XIE Hong-lan, XIAO Ti-qiao, XU Jun, LI Ting-ju. Influence of pulsed electric current on dendrite growth of Sn−Bi alloy via real-time observation [J]. Materials Science Forum, 2011, 675: 759−762.

[83] YANG Fen-fen, CHEN Zong-ning, CAO Fei, FAN Rong, KANG Hui-jun, HUANG Wan-xia, YUAN Qing-xi, XIAO Ti-qiao, FU Ya-nan, WANG Tong-min. Grain nucleation and growth behavior of a Sn−Pb alloy affected by direct current: An in situ investigation [J]. Journal of Materials Science & Technology, 2017, 33: 1134−1140.

[84] WANG Tong-min, ZHOU Peng, CAO Fei, KANG Hui-jun, CHEN Zong-ning, FU Ya-nan, XIAO Ti-qiao, HUANG Wan-xia, YUAN Qing-xi. Growth behavior of Cu_6Sn_5 in Sn−6.5Cu solders under DC considering trace Al: in situ observation [J]. Intermetallics, 2015, 58: 84−90.

[85] YANG Fen-fen, CAO Fei, LI Ren-geng, KANG Hui-jun, HUANG Wan-xia, WANG Tong-min. Study on the solidification of Sn−Pb alloy under direct current field by synchrotron X-ray radiography [J]. Materials Science Forum, 2016, 850: 186−190.

[86] XUAN Zhen-jing, MAO Feng, CAO Zhi-qiang, WANG Tong-min, ZOU Long-jiang. In situ observation on the solidification of Sn−10Cu hyperperitectic alloy under direct current field by synchrotron microradiography [J]. Journal of Alloys and Compounds, 2017, 721: 126−133.

[87] LIOTTI E, LUI A, VINCENT R, KUMAR S, GUO Z, CONNOLLEY T, DOLBNYA I P, HART M, ARNBERG L, MATHIESEN R H, GRANT P S. A synchrotron X-ray radiography study of dendrite fragmentation induced by a pulsed electromagnetic field in an Al−15Cu alloy [J]. Acta Materialia, 2014, 70: 228−239.

[88] WANG J, FAUTRELLE Y, REN Z M, NGUYEN-THI H, JAOUDE G S A, REINHART G, MANGELINCK-NOËL N, LI X, KALDRE I. Thermoelectric magnetic flows in melt during directional solidification [J]. Applied Physics Letters, 2014, 104: 121916.

[89] LIOTTI E, LUI A, KUMAR S, GUO Z, BI C, CONNOLLEY T, GRANT P S. The spatial and temporal distribution of dendrite fragmentation in solidifying Al−Cu alloys under different conditions [J]. Acta Materialia, 2016, 121: 384−395.

[90] CAO Fei, YANG Fen-fen, KANG Hui-jun, ZOU Long-jiang, XIAO Ti-qiao, HUANG Wan-xia, WANG Tong-min. Effect of traveling magnetic field on solute distribution and dendritic growth in unidirectionally solidifying Sn−50wt.%Pb alloy: An in situ observation [J]. Journal of Crystal Growth, 2016, 450: 91−95.

[91] XU Yan-jin, WEI Li-jun, HAN Bao-shuai, GUO En-yu, WANG Ming-yue, SU Yan-qing. Effect of a traveling magnetic field on micropore formation in Al−Cu alloys [J]. Metals, 2018, 8: 448.

[92] LEE T L, KHONG J C, FEZZAA K, MI J W. Ultrafast X-ray imaging and modelling of ultrasonic cavitations in liquid metal [J]. Materials Science Forum, 2013, 765: 190−194.

[93] MI J W, TAN D Y, LEE T L. In situ synchrotron X-ray study of ultrasound cavitation and its effect on solidification microstructures [J]. Metallurgical and Materials Transactions B, 2015, 46: 1615−1619.

[94] HUANG Hai-jun, SHU Da, FU Ya-nan, WANG Jun, SUN Bao-de. Synchrotron radiation x-ray imaging of cavitation bubbles in Al−Cu alloy melt [J]. Ultrasonics Sonochemistry, 2014, 21: 1275−1278.

[95] TAN D Y, LEE T L, KHONG J C, CONNOLLEY T, FEZZAA K, MI J W. High-speed synchrotron X-ray imaging studies of the ultrasound shockwave and enhanced flow during metal solidification processes [J]. Metallurgical and Materials Transactions A, 2015, 46: 2851−2861.

[96] NAGIRA T, NAKATSUKA N, YASUDA H, UESUGI K, TAKEUCHI A, SUZUKI Y. Impact of melt convection induced by ultrasonic wave on dendrite growth in Sn−Bi alloys [J]. Materials Letters, 2015, 150: 135−138.

[97] TZANAKIS I, XU W W, LEBON G S B, ESKIN D G, PERICLEOUS K, LEE P D. In situ synchrotron radiography and spectrum analysis of transient cavitation bubbles in molten aluminium alloy [J]. Physics Procedia, 2015, 70: 841−845.

[98] XU W W, TZANAKIS I, SRIRANGAM P, MIRIHANAGE W U, ESKIN D G, BODEY A J, LEE P D. Synchrotron quantification of ultrasound cavitation and bubble dynamics in Al−10Cu melts [J]. Ultrasonics Sonochemistry, 2016, 31: 355−361.

[99] WANG F, ESKIN D, MI J W, WANG C N, KOE B, KING A, REINHARD C, CONNOLLEY T. A synchrotron X-radiography study of the fragmentation and refinement of primary intermetallic particles in an Al−35Cu alloy induced by ultrasonic melt processing [J]. Acta Materialia, 2017, 141: 142−153.

[100] WANG F, TZANAKIS I, ESKIN D, MI J W, CONNOLLEY T. In situ observation of ultrasonic cavitation-induced fragmentation of the primary crystals formed in Al alloys [J]. Ultrasonics Sonochemistry, 2017, 39: 66−76.

[101] WANG B, TAN D Y, LEE T L, KHONG J C, WANG F, ESKIN D, CONNOLLEY T, FEZZAA K, MI J W. Ultrafast synchrotron X-ray imaging studies of microstructure fragmentation in solidification under ultrasound [J]. Acta Materialia, 2018, 144: 505−515.

[102] ZHANG Z G, WANG C N, KOE B, SCHLEPÜTZ C M, IRVINE S, MI J W. Synchrotron X-ray imaging and ultrafast tomography in situ study of the fragmentation and growth dynamics of dendritic microstructures in solidification under ultrasound [J]. Acta Materialia, 2021, 209: 116796.

[103] LUO S J, KEUNG W C, KANG Y L. Theory and application research development of semi-solid forming in China [J]. Transactions of Nonferrous Metals Society of China, 2010, 20: 1805−1814.

[104] QI Ming-fan, KANG Yong-lin, XU Yu-zhao, LI Jing-yuan, LIU Ai-sen. New technique for preparing A356 alloy semisolid slurry and its rheo-diecast microstructure and properties [J]. Transactions of Nonferrous Metals Society of China, 2021, 31: 1868−1884.

[105] GUAN Ren-guo, WEN Jing-lin, WANG Shun-cheng, LIU Xiang-hua. Microstructure behavior and metal flow during continuously extending-extrusion forming of semisolid A2017 alloy [J]. Transactions of Nonferrous Metals Society of China, 2006, 16: 382−386.

[106] SHANG Shu-zhen, LU Gui-min, TANG Xiao-ling, ZHAO Zu-xin, WU Cheng-ming. Deformation mechanism and forming properties of 6061Al alloys during compression in semi-solid state [J]. Transactions of Nonferrous Metals Society of China, 2010, 20: 1725−1730.

[107] CAI B, KARAGADDE S, ROWLEY D, MARROW T J, CONNOLLEY T, LEE P D. Time-resolved synchrotron tomographic quantification of deformation-induced flow in a semi-solid equiaxed dendritic Al−Cu alloy [J]. Scripta Materialia, 2015, 103: 69−72.

[108] PHILLION A B, HAMILTON R W, FULORIA D, LEUNG A C L, ROCKETT P, CONNOLLEY T, LEE P D. In situ X-ray observation of semi-solid deformation and failure in Al-Cu alloys [J]. Acta Materialia, 2011, 59: 1436−1444.

[109] FONSECA J, O'SULLIVAN C, NAGIRA T, YASUDA H, GOURLAY C M. In situ study of granular micromechanics in semi-solid carbon steels [J]. Acta Materialia, 2013, 61: 4169−4179.

[110] GOURLAY C M, NAGIRA T, DAHLE A K, NAKATSUKA N, UESUGI K, YASUDA H. Synchrotron radiography of direct-shear in semi-solid alloys [J]. IOP Conference Series: Materials Science and Engineering, 2012, 27: 012086.

[111] SU T C, O'SULLIVAN C, NAGIRA T, YASUDA H, GOURLAY C M. Semi-solid deformation of Al−Cu alloys: A quantitative comparison between real-time imaging and coupled LBM-DEM simulations [J]. Acta Materialia, 2019, 163: 208−225.

[112] CAI B, KARAGADDE S, YUAN L, MARROW T J, CONNOLLEY T, LEE P D. In situ synchrotron tomographic quantification of granular and intragranular deformation during semi-solid compression of an equiaxed dendritic Al−Cu alloy [J]. Acta Materialia, 2014, 76: 371−380.

[113] CAI B, KARAGADDE S, MARROW T J, CONNOLLEY T, LEE P D. Synchrotron X-ray tomographic quantification of deformation induced strain localisation in semi-solid Al−15wt.%Cu [C]//IOP Conference Series: Materials Science and Engineering, 2015, 84: 012079.

[114] BHAGAVATH S, CAI B, ATWOOD R, LI M, GHAFFARI B, LEE P D, KARAGADDE S. Combined deformation and solidification-driven porosity formation in aluminum alloys [J]. Metallurgical and Materials Transactions A, 2019, 50: 4891−4899.

[115] KAREH K M, LEE P D, ATWOOD R C, CONNOLLEY T, GOURLAY C M. Pore behaviour during semi-solid alloy compression: Insights into defect creation under pressure [J]. Scripta Materialia, 2014, 89: 73−76.

[116] KAREH K M, LEE P D, ATWOOD R C, CONNOLLEY T, GOURLAY C M. Revealing the micromechanisms behind semi-solid metal deformation with time-resolved X-ray tomography [J]. Nature Communications, 2014, 5: 4464.

[117] KARAGADDE S, LEE P D, CAI B, FIFE J L, AZEEM M A, KAREH K M, PUNCREOBUTR C, TSIVOULAS D,

CONNOLLEY T, ATWOOD R C. Transgranular liquation cracking of grains in the semi-solid state [J]. Nature Communications, 2015, 6: 8300.

[118] WANG W, GUO E Y, PHILLION A B, ESKIN D G, WANG T M, LEE P D. Semi-solid compression of nano/micro-particle reinforced Al−Cu composites: An in situ synchrotron tomographic study [J]. Materialia, 2020, 12: 100817.

[119] NAGIRA T, YASUDA H, UNOKI R, MORISHITA K, SUGIYAMA A, YOSHIYA M, UESUGI K. In situ observations of tensile and compressive deformations in semi solid metallic alloys using time-resolved X-ray imaging [J]. Tetsu-to-Hagane, 2017, 103: 668−677.

[120] TERZI S, SALVO L, SUËRY M, LIMODIN N, ADRIEN J, MAIRE E, PANNIER Y, BORNERT M, BERNARD D, FELBERBAUM M, RAPPAZ M, BOLLER E. In situ X-ray tomography observation of inhomogeneous deformation in semi-solid aluminium alloys [J]. Scripta Materialia, 2009, 61: 449−452.

[121] SISTANINIA M, TERZI S, PHILLION A B, DREZET J M, RAPPAZ M. 3-D granular modeling and in situ X-ray tomographic imaging: A comparative study of hot tearing formation and semi-solid deformation in Al−Cu alloys [J]. Acta Materialia, 2013, 61: 3831−3841.

[122] PUNCREOBUTR C, LEE P D, HAMILTON R W, CAI B, CONNOLLEY T. Synchrotron tomographic characterization of damage evolution during aluminum alloy solidification [J]. Metallurgical and Materials Transactions A, 2013, 44: 5389−5395.

[123] GE Xuan, XU Xiao-wei, HU Qiao-dan, LU Wen-quan, YANG Liang, CAO Sheng, XIA Ming-xu, LI Jian-guo. Ambiguous temperature difference in aerodynamic levitation process: Modelling, solving and application [J]. Journal of Materials Science & Technology, 2019, 35: 1636−1643.

[124] LU Wen-quan, ZHANG Shu-guang, LI Jian-guo. Segregation driven by collision and coagulation of minor droplets in Al−Bi immiscible alloys under aerodynamic levitation condition [J]. Materials Letters, 2013, 107: 340−343.

[125] ARAI Y, AOYAMA T, YODA S. Spherical sapphire single-crystal synthesis by aerodynamic levitation with high growth rate [J]. Review of Scientific Instruments, 2004, 75: 2262−2265.

[126] ARAI Y, PARADIS P F, AOYAMA T, ISHIKAWA T, YODA S. An aerodynamic levitation system for drop tube and quenching experiments [J]. Review of Scientific Instruments, 2003, 74: 1057−1063.

[127] ZHANG S G, ZHANG L, LU W Q, ZHANG W, YU J D, FU Y N, LI J G. Observation of bubble-involving spontaneous gas dissolution in superheated Al alloy melt [J]. Applied Physics Letters, 2013, 103: 164103.

[128] LU Wen-quan, ZHANG Shu-guang, LI Jian-guo. Observation of Bi coarsening and dissolution behaviors in melting Al−Bi immiscible alloy [J]. Acta Metallurgica Sinica (English Letters), 2016, 29: 800−803.

[129] LU W Q, ZHANG S G, ZHANG W, KAPTAY G, YU J D, FU Y N, LI J G. Direct observation of the segregation driven by bubble evolution and liquid phase separation in Al−10wt.%Bi immiscible alloy [J]. Scripta Materialia, 2015, 102: 19−22.

[130] LU Wen-quan, ZHANG Shu-guang, ZHANG Wei, HU Qiao-dan, YU Jian-ding, FU Ya-nan, LI Jian-guo. A full view of the segregation evolution in Al−Bi immiscible alloy [J]. Metallurgical and Materials Transactions A, 2017, 48: 2701−2705.

[131] LU Wen-quan, ZHANG Shu-guang, ZHANG Wei, LI Jian-guo. Imaging of structure evolution in solidifying Al−Bi immiscible alloys by synchrotron radiography [J]. Journal of Materials Science & Technology, 2016, 32: 1321−1325.

[132] ZHAO Lei, LIAO Heng-cheng, PAN Ye, WANG Lin, WANG Qi-gui. Abnormal macrosegregation induced by formed porosity during solidification of an Al−Sn alloy [J]. Scripta Materialia, 2011, 65: 795−798.

[133] LU Wen-quan, HU Qiao-dan, ZHANG Wei, LI Jian-guo. Dynamic behaviors of minor droplets and the role of bubbles in phase-separating Al−Bi immiscible alloy [J]. Journal of Molecular Liquids, 2020, 320: 114478.

[134] MASSALSKI T B. Binary alloy phase diagrams [M]. Vol. 3, ASM International, 1990.

[135] LEUNG C L A, MARUSSI S, ATWOOD R C, TOWRIE M, WITHERS P J, LEE P D. In situ X-ray imaging of defect and molten pool dynamics in laser additive manufacturing [J]. Nature Communications, 2018, 9: 1355.

[136] GUO N N, LEU M C. Additive manufacturing: Technology, applications and research needs [J]. Frontiers of Mechanical Engineering, 2013, 8: 215−243.

[137] CHEN Lian, HE Yong, YANG Ying-xin, NIU Shi-wei, REN Hai-tao. The research status and development trend of additive manufacturing technology [J]. The International Journal of Advanced Manufacturing Technology, 2017, 89: 3651−3660.

[138] OSAKADA K, SHIOMI M. Flexible manufacturing of metallic products by selective laser melting of powder [J]. International Journal of Machine Tools and Manufacture 2006, 46: 1188−1193.

[139] DUTTA B, SINGH V, NATU H, CHOI J, MAZUMDER J. Direct metal deposition [J]. Advanced Materials and Processes, 2009, 167: 29−31.

[140] CHAM J G, BAILEY S A, CLARK J E, FULL R J, CUTKOSKY M R. Fast and robust: Hexapedal robots via shape deposition manufacturing [J]. The International Journal of Robotics Research, 2002, 21: 869−882.

[141] WANG Hua-ming. Materials' fundamental issues of laser additive manufacturing for high-performance large metallic components [J]. Acta Aeronautica et Astronautica Sinica, 2014, 35: 2690−2698. (in Chinese)

[142] ZHAO C, FEZZAA K, CUNNINGHAM R W, WEN H D, DE CARLO F, CHEN L Y, ROLLETT A D, SUN T. Real-time monitoring of laser powder bed fusion process using high-speed X-ray imaging and diffraction [J]. Scientific Reports, 2017, 7: 3602.

[143] CUNNINGHAM R, ZHAO C, PARAB N, KANTZOS C, PAUZA J, FEZZAA K, SUN T, ROLLETT A D. Keyhole threshold and morphology in laser melting revealed by ultrahigh-speed x-ray imaging [J]. Science, 2019, 363: 849−852.

[144] ZHAO C, PARAB N D, LI X X, FEZZAA K, TAN W D, ROLLETT A D, SUN T. Critical instability at moving keyhole tip generates porosity in laser melting [J]. Science, 2020, 370: 1080−1086.

[145] HOJJATZADEH S M H, PARAB N D, GUO Q L, QU M L,

XIONG L H, ZHAO C, ESCANO L I, FEZZAA K, EVERHART W, SUN T, CHEN L Y. Direct observation of pore formation mechanisms during LPBF additive manufacturing process and high energy density laser welding [J]. International Journal of Machine Tools and Manufacture, 2020, 153: 103555.

[146] MARTIN A A, CALTA N P, KHAIRALLAH S A, WANG J, DEPOND P J, FONG A Y, THAMPY V, GUSS G M, KISS A M, STONE K H, TASSONE C J, NELSON WEKER J N, TONEY M F, von BUUREN T, MATTHEWS M J. Dynamics of pore formation during laser powder bed fusion additive manufacturing [J]. Nature Communications, 2019, 10: 1987.

[147] MARTIN A A, CALTA N P, HAMMONS J A, KHAIRALLAH S A, NIELSEN M H, SHUTTLESWORTH R M, SINCLAIR N, MATTHEWS M J, JEFFRIES J R, WILLEY T M, LEE J R I. Ultrafast dynamics of laser-metal interactions in additive manufacturing alloys captured by in situ X-ray imaging [J]. Materials Today Advances, 2019, 1: 100002.

[148] LEUNG C L A, MARUSSI S, TOWRIE M, ATWOOD R C, WITHERS P J, LEE P D. The effect of powder oxidation on defect formation in laser additive manufacturing [J]. Acta Materialia, 2019, 166: 294−305.

[149] LEUNG C L A, MARUSSI S, TOWRIE M, del val GARCIA J, ATWOOD R C, BODEY A J, JONES J L R, WITHERS P J, LEE P D. Laser-matter interactions in additive manufacturing of stainless steel SS316L and 13-93 bioactive glass revealed by in situ X-ray imaging [J]. Additive Manufacturing, 2018, 24: 647−657.

[150] GUO Q L, ZHAO C, QU M L, XIONG L H, ESCANO L I, HOJJATZADEH S M H, PARAB N D, FEZZAA K, EVERHART W, SUN T, CHEN L Y. In-situ characterization and quantification of melt pool variation under constant input energy density in laser powder bed fusion additive manufacturing process [J]. Additive Manufacturing, 2019, 28: 600−609.

[151] GUO Q L, ZHAO C, QU M L, XIONG L H, HOJJATZADEH S M H, ESCANO L I, PARAB N D, FEZZAA K, SUN T, CHEN L Y. In-situ full-field mapping of melt flow dynamics in laser metal additive manufacturing [J]. Additive Manufacturing, 2020, 31: 100939.

[152] CHEN Y H, CLARK S J, COLLINS D M, MARUSSI S, HUNT S A, FENECH D M, CONNOLLEY T, ATWOOD R C, MAGDYSYUK O V, BAXTER G J, JONES M A, LEUNG C L A, LEE P D. Correlative synchrotron X-ray imaging and diffraction of directed energy deposition additive manufacturing [J]. Acta Materialia, 2021, 209: 116777.

[153] CHEN Y H, CLARK S J, SINCLAIR L, LEUNG C L A, MARUSSI S, CONNOLLEY T, ATWOOD R C, BAXTER G J, JONES M A, TODD I, LEE P D. Synchrotron X-ray imaging of directed energy deposition additive manufacturing of titanium alloy Ti-6242 [J]. Additive Manufacturing, 2021, 41: 101969.

[154] CHEN Y H, CLARK S J, HUANG Y Z, SINCLAIR L, LEUNG C L A, MARUSSI S, CONNOLLEY T, MAGDYSYUK O V, ATWOOD R C, BAXTER G J, JONES M A, TODD I, LEE P D. In situ X-ray quantification of melt pool behaviour during directed energy deposition additive manufacturing of stainless steel [J]. Materials Letters, 2021, 286: 129205.

[155] CHEN Y, CLARK S, LEUNG A L, SINCLAIR L, MARUSSI S, ATWOOD R, CONNOLEY T, JONES M, BAXTER G, LEE P D. Melt pool morphology in directed energy deposition additive manufacturing process [J]. IOP Conference Series: Materials Science and Engineering, 2020, 861: 0120.

基于同步辐射成像技术的原位观察装置及金属凝固过程原位表征研究进展

卢温泉，张乃方，丁宗业，胡侨丹，李建国

上海交通大学 材料科学与工程学院，上海 200240

摘 要：金属材料的凝固过程对其最终显微组织和性能起着决定性的作用。因此，采用先进的原位表征技术探究金属的凝固过程具有重要意义。同步辐射 X 射线成像技术是直接观察金属凝固过程的有效手段。本文作者总结了与同步辐射光源相配套的凝固装置的发展，包括定向凝固装置、电阻炉、多场耦合装置、半固态成形装置、气动悬浮装置和激光增材制造装置。重点介绍了应用同步辐射 X 射线成像技术揭示不同原位环境下金属凝固行为的最新研究进展，并对该技术在凝固领域的前沿研究方向进行了展望。可以预见，同步辐射 X 射线成像技术的发展将在不同尺度上深入理解金属和其他材料的凝固过程发挥重要作用。

关键词：同步辐射成像；原位观察；凝固行为；凝固装置；金属材料

(Edited by Bing YANG)